Spin resonances in iron selenide high-T_c superconductors by proximity to a hidden spin density wave

J. P. Rodriguez

Department of Physics and Astronomy, California State University, Los Angeles, California 90032, USA

Recent inelastic neutron scattering studies by B. Pan *et al.* [Nat. Commun. **8**, 123 (2017)] find evidence for spin resonances in an iron selenide high-T_c superconductor that persist at energies above the quasiparticle gap. The momenta of such spin excitations form a diamond around the checkerboard wave vector, $\boldsymbol{Q}_{\mathrm{AF}}$, that is associated with the square lattice of iron atoms that makes up the system. It has been suggested that the "hollowed-out" spin-excitation spectrum is due to hidden Néel order. We study such a hidden spin density wave (hSDW) state that results from nested Fermi surfaces at the center and at the corner of the unfolded Brillouin zone. It emerges within mean-field theory from an extended Hubbard model over a square lattice of iron atoms that contain the minimal d_{xz} and d_{yz} orbitals. Opposing Néel order exists over the isotropic $d+ = d_{xz} + id_{yz}$ and $d- = d_{xz} - id_{yz}$ orbitals. The dynamical spin susceptibility of the hSDW is computed within the random phase approximation, at perfect nesting. Unobservable Goldstone modes that disperse acoustically are found at $\boldsymbol{Q}_{\mathrm{AF}}$. A threshold is found in the spectrum of observable spin excitations that forms a "floating ring" at $\boldsymbol{Q}_{\mathrm{AF}}$ also. The ring threshold moves down in energy toward zero with increasing Hund's rule coupling, while it moves up in energy with increasing magnetic frustration. Comparison with the normal-state features of the spin-excitation spectrum shown by electron-doped iron selenide is made. Also, recent predictions of a Lifshitz transition from the nested Fermi surfaces to Fermi surface pockets at the corner of the folded Brillouin zone will be discussed.

I. INTRODUCTION

Spin resonances inside the energy gap that opens at the Fermi level in the spectrum of quasiparticle excitations of high-temperature superconductors are commonly observed [1,2]. In the case of iron pnictide superconductors, they are predicted to exist just below the quasiparticle energy gap, $2\Delta_{\mathrm{SC}}$, at the nesting wave vector that connects hole-type Fermi surfaces at the center of the Brillouin zone with electron-type Fermi surfaces at the corner of the folded Brillouin zone [3,4]. Such predictions are based on S^{+-} Bardeen-Cooper-Schrieffer (BCS) ground states, where the sign of Cooper pairs alternates between the hole-type and the electron-type Fermi surfaces [5,6]. It is believed that low-energy spin fluctuations that arise from the nested Fermi surfaces are what bind together electrons into Cooper pairs in the S^{+-} state [7]. The predicted spin resonances inside of the energy gap, at the "stripe" spin density wave (SDW) wave vectors, have indeed been observed in iron pnictide superconductors by inelastic neutron scattering [2].

Spin resonances have also been observed inside the quasiparticle energy gap of electron-doped iron selenide high-temperature superconductors, but at wave numbers midway between the "stripe" SDW ones and the checkerboard one that describes Néel antiferromagnetism [8–12]. Electron doping buries the hole bands at the center of the Brillouin zone below the Fermi level, leaving only the electron-type Fermi surface pockets at the corner of the folded Brillouin zone [13–16]. Spin resonances are therefore observed in electron-doped iron selenide in the absence of nested Fermi surfaces, which is a puzzle. Additionally, recent inelastic neutron scattering studies of iron selenide that is electron-doped by intercalated

organic molecules find evidence for spin resonances that persist *above* the quasiparticle energy gap, $2\Delta_{\mathrm{SC}}$, at wave numbers that form a "diamond" around the checkerboard wave vector [11], $(\pi/a, \pi/a)$. Such relatively high-energy spin excitations very likely persist into the normal state at temperatures above T_c.

Recent theoretical work suggests that the "rings" and "diamonds" of spin excitations observed in electron-doped FeSe at the checkerboard wave vector are due to proximity to a hidden spin density wave (hSDW) state [17–19]. Here, the sign of the ordered magnetic moment alternates between the principal $d+ = (d_{xz} + id_{yz})/\sqrt{2}$ and $d- = (d_{xz} - id_{yz})/\sqrt{2}$ orbitals of the iron atom, as well as between the "white" and the "black" sites on the checkerboard of iron atoms [20,21]. It is the most isotropic one among a family of hSDW states that are related by isospin rotations [22]. The stability of the hSDW is driven by perfectly nested Fermi surfaces at the center and at the corner of the unfolded Brillouin zone. (See Fig. 1.) It has recently been shown by the author and a co-worker that fluctuation exchange with Goldstone modes associated with such hidden magnetic order results in a Lifshitz transition to electron/hole Fermi surface pockets at the corner of the folded Brillouin zone [19]. (See Fig. 3.) A rigid shift in energy of this renormalized electronic structure because of electron doping away from half filling can bury the hole pockets, leaving the electron pockets that are observed by angle-resolved photoemission spectroscopy (ARPES) in electron-doped iron selenide [22].

Below, we shall reveal the nature of spin excitations in the hidden SDW state within an extended Hubbard model over a square lattice of iron atoms that includes only the principal $3d_{xz}$ and $3d_{yz}$ orbitals of iron superconductors [19].

TABLE I. List of physical operators per site i according to spin and isospin quantum numbers, S and I. In the latter case, the $d+$ and $d-$ orbitals are analogous to the u and d quarks. (See Ref. [22].)

Physical quantity	Operator	S	I
Density	$n_{i,d+} + n_{i,d-}$	0	0
True spin	$\boldsymbol{S}_{i,d+} + \boldsymbol{S}_{i,d-}$	1	0
Hidden spin	$\boldsymbol{S}_{i,d+} - \boldsymbol{S}_{i,d-}$	1	1

In particular, the dynamical spin susceptibility is computed within a Nambu-Gorkov-type [23–25] random phase approximation (RPA) that accounts for perfect nesting of the unrenormalized Fermi surfaces mentioned above. This calculation is then the two-orbital realization of Schrieffer, Wen, and Zhang's "spin bag" calculation of the dynamical spin susceptibility for the conventional Hubbard model over the square lattice [26–29]. As expected, we recover the Goldstone modes that disperse acoustically from the nesting wave vector, $\boldsymbol{Q}_{\mathrm{AF}} = (\pi/a, \pi/a)$. Such modes have an extremely weak spectral weight in the true-spin channel, however. (See Table I.) A ring of spin excitations at $\boldsymbol{Q}_{\mathrm{AF}}$ begins at energies above the Goldstone modes in the true-spin channel, on the other hand. They evolve into a diamond shape at $\boldsymbol{Q}_{\mathrm{AF}}$ as energy increases above the threshold. We shall argue that the dynamical spin susceptibility within RPA accounts for spin excitations in the normal state of electron-doped iron selenide.

II. NESTED FERMI SURFACES IN HUBBARD MODEL

The extended Hubbard model for electron-doped iron selenide and the mean-field theory for the hidden SDW state are introduced below.

A. Electron hopping over square lattice of iron atoms

We keep the $3d_{xz}/3d_{yz}$ orbitals of the iron atoms in the following description of a single layer of heavily electron-doped FeSe. In particular, consider the isotropic basis of orbitals $d- = (d_{xz} - id_{yz})/\sqrt{2}$ and $d+ = (d_{xz} + id_{yz})/\sqrt{2}$. Kinetic dynamics is governed by the hopping Hamiltonian

$$H_{\mathrm{hop}} = -\sum_{\langle i,j \rangle} \left(t_1^{\alpha,\beta} c_{i,\alpha,s}^\dagger c_{j,\beta,s} + \mathrm{H.c.} \right)$$
$$- \sum_{\langle\langle i,j \rangle\rangle} \left(t_2^{\alpha,\beta} c_{i,\alpha,s}^\dagger c_{j,\beta,s} + \mathrm{H.c.} \right), \quad (1)$$

where the repeated indices α and β are summed over the $d-$ and $d+$ orbitals, where the repeated index s is summed over

electron spin $\uparrow$ and $\downarrow$, and where $\langle i, j \rangle$ and $\langle\langle i, j \rangle\rangle$ represent nearest-neighbor (1) and next-nearest-neighbor (2) links on the square lattice of iron atoms. Above, $c_{i,\alpha,s}$ and $c_{i,\alpha,s}^\dagger$ denote annihilation and creation operators for an electron of spin s in orbital α at site i. The reflection symmetries in a single layer of FeSe imply that the above intraorbital and interorbital hopping matrix elements show s-wave and d-wave symmetry, respectively [30–32]. Nearest neighbor hopping matrix elements satisfy

$$t_1^{\pm\pm}(\hat{\mathbf{x}}) = t_1^{\parallel} = t_1^{\pm\pm}(\hat{\mathbf{y}}),$$
$$t_1^{\pm\mp}(\hat{\mathbf{x}}) = t_1^{\perp} = -t_1^{\pm\mp}(\hat{\mathbf{y}}), \quad (2)$$

with real $t_1^{\parallel}$ and $t_1^{\perp}$, while next-nearest-neighbor hopping matrix elements satisfy

$$t_2^{\pm\pm}(\hat{\mathbf{x}} + \hat{\mathbf{y}}) = t_2^{\parallel} = t_2^{\pm\pm}(\hat{\mathbf{y}} - \hat{\mathbf{x}}),$$
$$t_2^{\pm\mp}(\hat{\mathbf{x}} + \hat{\mathbf{y}}) = \pm t_2^{\perp} = -t_2^{\pm\mp}(\hat{\mathbf{y}} - \hat{\mathbf{x}}), \quad (3)$$

with real $t_2^{\parallel}$ and pure-imaginary $t_2^{\perp}$.

The above hopping Hamiltonian is diagonalized [19] by plane waves of $d_{x(\delta)z}$ and $id_{y(\delta)z}$ orbitals that are rotated with respect to the principal axis by a phase shift $\delta(\boldsymbol{k})$:

$$|\boldsymbol{k}, d_{x(\delta)z}\rangle\rangle = \mathcal{N}^{-1/2} \sum_i e^{i\boldsymbol{k}\cdot\boldsymbol{r}_i} [e^{i\delta(\boldsymbol{k})}|i, d+\rangle + e^{-i\delta(\boldsymbol{k})}|i, d-\rangle],$$

$$i|\boldsymbol{k}, d_{y(\delta)z}\rangle\rangle = \mathcal{N}^{-1/2} \sum_i e^{i\boldsymbol{k}\cdot\boldsymbol{r}_i} [e^{i\delta(\boldsymbol{k})}|i, d+\rangle - e^{-i\delta(\boldsymbol{k})}|i, d-\rangle],$$

$$(4)$$

where $\mathcal{N} = 2N_{\mathrm{Fe}}$ is the number of iron site orbitals. The energy eigenvalue of the (bonding) $d_{x(\delta)z}$ band is given by $\varepsilon_+(\boldsymbol{k}) = \varepsilon_{\parallel}(\boldsymbol{k}) + |\varepsilon_{\perp}(\boldsymbol{k})|$ and the energy eigenvalue of the (anti-bonding) $d_{y(\delta)z}$ band is given by $\varepsilon_-(\boldsymbol{k}) = \varepsilon_{\parallel}(\boldsymbol{k}) - |\varepsilon_{\perp}(\boldsymbol{k})|$, where

$$\varepsilon_{\parallel}(\boldsymbol{k}) = -2t_1^{\parallel}(\cos k_x a + \cos k_y a) - 2t_2^{\parallel}(\cos k_+ a + \cos k_- a),$$
$$(5a)$$

$$\varepsilon_{\perp}(\boldsymbol{k}) = -2t_1^{\perp}(\cos k_x a - \cos k_y a) - 2t_2^{\perp}(\cos k_+ a - \cos k_- a)$$
$$(5b)$$

are diagonal and off-diagonal matrix elements, with $k_{\pm} = k_x \pm k_y$. The phase shift $\delta(\boldsymbol{k})$ is set by $\varepsilon_{\perp}(\boldsymbol{k}) = |\varepsilon_{\perp}(\boldsymbol{k})|e^{i2\delta(\boldsymbol{k})}$, with

$$\cos 2\delta(\boldsymbol{k}) = \frac{-t_1^{\perp}(\cos k_x a - \cos k_y a)}{\sqrt{t_1^{\perp 2}(\cos k_x a - \cos k_y a)^2 + |2t_2^{\perp}|^2(\sin k_x a)^2(\sin k_y a)^2}}, \quad (6a)$$

$$\sin 2\delta(\boldsymbol{k}) = \frac{2(t_2^{\perp}/i)(\sin k_x a)(\sin k_y a)}{\sqrt{t_1^{\perp 2}(\cos k_x a - \cos k_y a)^2 + |2t_2^{\perp}|^2(\sin k_x a)^2(\sin k_y a)^2}}. \quad (6b)$$

At $\boldsymbol{k} = 0$ and $\boldsymbol{Q}_{\mathrm{AF}}$, the matrix element $\varepsilon_{\perp}(\boldsymbol{k})$ vanishes. The phase factor $e^{i2\delta(\boldsymbol{k})}$ is then notably singular there.

Now turn off next-nearest-neighbor intraorbital hopping: $t_2^{\parallel} = 0$. The above energy bands then satisfy the perfect nest-
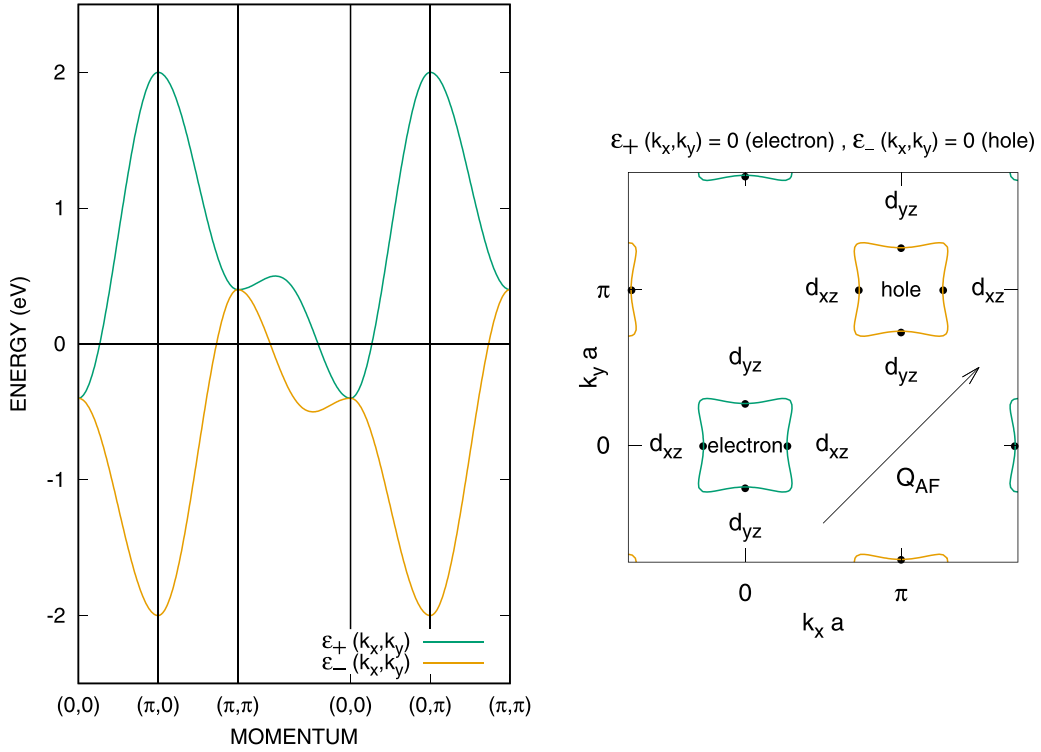
FIG. 1. Band structure with perfectly nested Fermi surfaces at half filling: $\varepsilon_+(\boldsymbol{k}) = 0$ and $\varepsilon_-(\boldsymbol{k}) = 0$, with hopping matrix elements $t_1^{\parallel} = 100$ meV, $t_1^{\perp} = 500$ meV, $t_2^{\parallel} = 0$, and $t_2^{\perp} = 100i$ meV. Dirac cones emerge from the dots on the Fermi surfaces in the hSDW state.

ing condition [19]

$$\varepsilon_\pm(\boldsymbol{k} + \boldsymbol{Q}_{\mathrm{AF}}) = -\varepsilon_\mp(\boldsymbol{k}), \tag{7}$$

where $\boldsymbol{Q}_{\mathrm{AF}} = (\pi/a, \pi/a)$ is the Néel ordering vector on the square lattice of iron atoms. As a result, the Fermi level at half filling lies at $\epsilon_{\mathrm{F}} = 0$. Figure 1 shows such perfectly nested electron-type and hole-type Fermi surfaces for hopping parameters $t_1^{\parallel} = 100$ meV, $t_1^{\perp} = 500$ meV, $t_2^{\parallel} = 0$, and $t_2^{\perp} = 100i$ meV.

B. Extended Hubbard model

Next, add interactions due to on-site Coulomb repulsion and superexchange interactions [33,34] via the Se atoms to the hopping Hamiltonian (1): $H = H_{\mathrm{hop}} + H_U + H_{\mathrm{sprx}}$. The second term counts on-site Coulomb repulsion [35],

$$H_U = \sum_i [U_0 n_{i,\alpha,\uparrow} n_{i,\alpha,\downarrow} + J_0 \boldsymbol{S}_{i,d-} \cdot \boldsymbol{S}_{i,d+}$$
$$+ U_0' n_{i,d+} n_{i,d-} + J_0'(c_{i,d+,\uparrow}^\dagger c_{i,d+,\downarrow}^\dagger c_{i,d-,\downarrow} c_{i,d-,\uparrow} + \mathrm{H.c.})], \tag{8}$$

where $n_{i,\alpha,s} = c_{i,\alpha,s}^\dagger c_{i,\alpha,s}$ is the occupation operator, where $\boldsymbol{S}_{i,\alpha} = \frac{\hbar}{2} \sum_{s,s'} c_{i,\alpha,s}^\dagger \boldsymbol{\sigma}_{s,s'} c_{i,\alpha,s'}$ is the spin operator, and where $n_{i,\alpha} = n_{i,\alpha,\uparrow} + n_{i,\alpha,\downarrow}$. Above, $U_0 > 0$ denotes the intraorbital on-site Coulomb repulsion energy, while $U_0' > 0$ denotes the interorbital one. Also, $J_0 < 0$ is the ferromagnetic Hund's rule exchange coupling constant, while J_0' is the matrix element for on-site Josephson tunneling between orbitals.

The last term in the Hamiltonian represents superexchange interactions [33,34] among the iron spins via the selenium atoms:

$$H_{\mathrm{sprx}} = \sum_{\langle i,j \rangle} J_1 (\boldsymbol{S}_{i,d-} + \boldsymbol{S}_{i,d+}) \cdot (\boldsymbol{S}_{j,d-} + \boldsymbol{S}_{j,d+})$$
$$+ \sum_{\langle\langle i,j \rangle\rangle} J_2 (\boldsymbol{S}_{i,d-} + \boldsymbol{S}_{i,d+}) \cdot (\boldsymbol{S}_{j,d-} + \boldsymbol{S}_{j,d+}). \tag{9}$$

Above, J_1 and J_2 are positive superexchange coupling constants across nearest-neighbor and next-nearest-neighbor iron sites. Assume henceforth that magnetic frustration is moderate to strong: $J_2 > 0.5 J_1$. In isolation, and at strong on-site-orbital repulsion, H_{sprx} thereby favors "stripe" SDW order over conventional Néel order.

III. HIDDEN SPIN DENSITY WAVE

The perfectly nested Fermi surfaces shown by Fig. 1 will result in a spin density wave state within the previous extended Hubbard model at ordering wave vector $\boldsymbol{Q}_{\mathrm{AF}} = (\pi/a, \pi/a)$. In the present $d-/d+$ basis of d_{xz}/d_{yz} orbitals, the most natural candidates are the true spin density wave $(0, \pi, \pi)$ and the hidden spin density wave (π, π, π), with the ordered moments

$$\mathcal{N}^{-1} \sum_i e^{i\boldsymbol{Q}_{\mathrm{AF}} \cdot \boldsymbol{r}_i} \sum_{s=\uparrow,\downarrow} (\mathrm{sgn}\, s) \frac{\hbar}{2} \langle c_{i,d+,s}^\dagger c_{i,d+,s} \pm c_{i,d-,s}^\dagger c_{i,d-,s} \rangle. \tag{10}$$

It is important to recall that the creation/annihilation operators transform as

$$c_{i,d\pm,s}^\dagger \to e^{\pm i\phi} c_{i,d\pm,s}^\dagger \quad \text{and} \quad c_{i,d\pm,s} \to e^{\mp i\phi} c_{i,d\pm,s}$$

TABLE II. List of hidden-order magnetic moments by isospin quantization axis. Examples of where such hidden SDW order parameters appear in the literature are also listed.

hSDW ordered moment	Isospin axis	Reference
$(\text{sgn } s)(c_{i,d_{xz},s}^{\dagger} c_{i,d_{xz},s} - c_{i,d_{yz},s}^{\dagger} c_{i,d_{yz},s}) e^{i\boldsymbol{Q}_{\text{AF}} \cdot \boldsymbol{r}_i}$	I_1	None
$(\text{sgn } s)(c_{i,d_{xz},s}^{\dagger} c_{i,d_{yz},s} + c_{i,d_{yz},s}^{\dagger} c_{i,d_{xz},s}) e^{i\boldsymbol{Q}_{\text{AF}} \cdot \boldsymbol{r}_i}$	I_2	Berg, Metlitski, and Sachdev [38]
$(\text{sgn } s)i(c_{i,d_{xz},s}^{\dagger} c_{i,d_{yz},s} - c_{i,d_{yz},s}^{\dagger} c_{i,d_{xz},s}) e^{i\boldsymbol{Q}_{\text{AF}} \cdot \boldsymbol{r}_i}$	I_3	Rodriguez [17]

under a rotation of the orbitals by an angle ϕ about the z axis. The ordered moments (10) of both the true SDW (+) and of the hidden SDW (−) are then notably isotropic with respect to such rotations. Neither SDW state therefore couples to nematic instabilities that can appear in the phase diagram of iron superconductors [36,37].

Consider, now, the $d-$ and $d+$ orbitals as components of isospin [22] $I = 1/2$. In general, the ordered moment of an hSDW state has isospin $I = 1$. (See Table I.) In particular, they are components of the tensor product

$$\mathcal{N}^{-1} \sum_i e^{i\boldsymbol{Q}_{\text{AF}} \cdot \boldsymbol{r}_i} \sum_{s,s'=\uparrow,\downarrow} \boldsymbol{\sigma}_{s,s'} \sum_{\alpha,\alpha'=d-,d+} \boldsymbol{\tau}_{\alpha,\alpha'} \frac{\hbar}{2} \langle c_{i,\alpha,s}^{\dagger} c_{i,\alpha',s'} \rangle, \tag{11}$$

where $\boldsymbol{\sigma}$ and $\boldsymbol{\tau}$ are Pauli matrices. The candidate hSDW state (10), for example, corresponds to the tensor product $\sigma_3 \tau_3$. Table II lists the ordered magnetic moments of such hSDW states along the three principal axes of the isospin $\boldsymbol{I}$. Notice the hSDW state along the I_2 isospin axis that was introduced by Berg, Metlitski, and Sachdev in the context of copper oxide high-temperature superconductors [38]. Both it and the hSDW state along the I_1 isospin axis are *not*, in fact, isotropic about the orbital z axis. Below, we shall review the mean-field theory for the candidate hSDW state [19] (10) along the I_3 isospin axis. Both it (−) and the true SDW state (+) provide the basis for the RPA calculation in the next section.

A. Mean-field theory

Assume that the expectation value of the magnetic moment per site, per orbital, shows hidden Néel order, with spontaneous symmetry breaking along the z axis:

$$\langle m_{i,\alpha} \rangle = (-1)^{\alpha} e^{i\boldsymbol{Q}_{\text{AF}} \cdot \boldsymbol{r}_i} \langle m_{0,0} \rangle, \tag{12}$$

where $\langle m_{i,\alpha} \rangle = \frac{1}{2} \langle n_{i,\alpha,\uparrow} \rangle - \frac{1}{2} \langle n_{i,\alpha,\downarrow} \rangle$. (Henceforth, set $\hbar = 1$.) Such an hSDW state (−) is expected to be more stable than the true SDW state (+) in the presence of magnetic frustration [21], $J_1, J_2 > 0$. Also, calculations in the local-moment limit find that the above hidden magnetic order is more stable than the "stripe" SDW mentioned previously at weak to moderate strength in the Hund's rule coupling [17,21]. The superexchange terms, H_{sprx}, make no contribution within the mean-field approximation, since the net magnetic moment per iron atom is null in the hidden-order Néel state. Also, the formation of a spin singlet per iron site orbital is suppressed at the strong-coupling limit, $U_0 \to \infty$. The on-site-orbital Josephson tunneling term (J_0') in H_U can then be neglected on that basis. We are then left with the two on-iron-site repulsion terms and the Hund's rule term in H_U.

The mean-field replacement of the intraorbital on-site term (U_0) is the usual one [26]:

$$n_{i,\alpha,\uparrow} n_{i,\alpha,\downarrow} \to \frac{1}{2} \langle n_{i,\alpha} \rangle (n_{i,\alpha,\uparrow} + n_{i,\alpha,\downarrow}) - \langle m_{i,\alpha} \rangle (n_{i,\alpha,\uparrow} - n_{i,\alpha,\downarrow})$$
$$- \langle n_{i,\alpha,\uparrow} \rangle \langle n_{i,\alpha,\downarrow} \rangle.$$

The first term above can be absorbed into the chemical potential and the last term above is a constant-energy shift. This leaves a mean-field contribution to the Hamiltonian: $-\sum_i \sum_{\alpha} U_0 \langle m_{i,\alpha} \rangle (n_{i,\alpha,\uparrow} - n_{i,\alpha,\downarrow})$. A similar mean-field replacement of the interorbital on-iron-site repulsion term (U_0') in H_U can be entirely absorbed into a shift of the chemical potential plus a constant-energy shift [19], on the other hand. Finally, we make the same type of mean-field replacement for the Hund's rule term (J_0) in H_U:

$$\boldsymbol{S}_{i,d+} \cdot \boldsymbol{S}_{i,d-} \to S_{i,d+}^{(z)} \langle S_{i,d-}^{(z)} \rangle + \langle S_{i,d+}^{(z)} \rangle S_{i,d-}^{(z)} - \langle S_{i,d+}^{(z)} \rangle \langle S_{i,d-}^{(z)} \rangle.$$

Again, the last term above is a constant-energy shift. The first two terms, however, contribute to the mean-field Hamiltonian: $\sum_i \sum_{\alpha} \frac{1}{2} J_0 \langle m_{i,\bar{\alpha}} \rangle (n_{i,\alpha,\uparrow} - n_{i,\alpha,\downarrow})$, which is equal to $-\sum_i \sum_{\alpha} \frac{1}{2} J_0 \langle m_{i,\alpha} \rangle (n_{i,\alpha,\uparrow} - n_{i,\alpha,\downarrow})$ in the case of hidden magnetic order (12). Here, $\overline{d\pm} = d\mp$.

Neglecting on-site-orbital Josephson tunneling (J_0'), the net contribution to the mean-field Hamiltonian from interactions in the present two-orbital Hubbard model is then

$$-\sum_i \sum_{\alpha} U(\pi) \langle m_{i,\alpha} \rangle (n_{i,\alpha,\uparrow} - n_{i,\alpha,\downarrow})$$
$$= -\langle m_{0,0} \rangle U(\pi) \sum_i \sum_{\alpha} (-1)^{\alpha} e^{i\boldsymbol{Q}_{\text{AF}} \cdot \boldsymbol{r}_i} (n_{i,\alpha,\uparrow} - n_{i,\alpha,\downarrow}),$$

where

$$U(\pi) = U_0 + \frac{1}{2} J_0. \tag{13}$$

Notice that the sum on the right-hand side above over sites and over orbitals is twice the hidden-order moment $S_z(\pi, \boldsymbol{Q}_{\text{AF}})$. (See Appendix A.) Reexpressing it in the band basis (4) and then applying the identity (31) for the phase shift ultimately yields the mean-field Hamiltonian for the present two-orbital Hubbard model [19]:

$$H^{(mf)} = \sum_s \sum_{\boldsymbol{k}} \sum_{n=1,2} \varepsilon_n(\boldsymbol{k}) c_s^{\dagger}(n, \boldsymbol{k}) c_s(n, \boldsymbol{k})$$
$$\mp \sum_s \sum_{\boldsymbol{k}} [(\text{sgn } s) \Delta(\boldsymbol{k}) c_s^{\dagger}(1, \bar{\boldsymbol{k}}) c_s(2, \boldsymbol{k}) + \text{H.c.}], \tag{14}$$

where $\bar{\boldsymbol{k}} = \boldsymbol{k} + \boldsymbol{Q}_{\text{AF}}$, with a gap function

$$\Delta(\boldsymbol{k}) = \Delta_0 \sin[2\delta(\boldsymbol{k})], \tag{15}$$

where

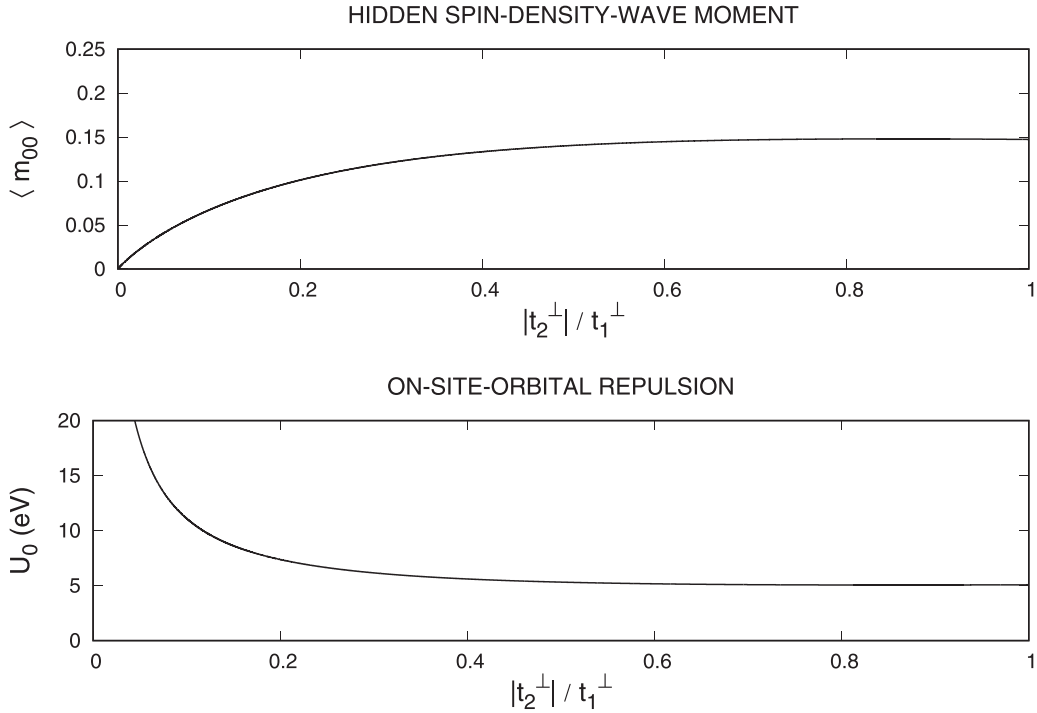$$\Delta_0 = \langle m_{0,0} \rangle U(\pi). \tag{16}$$

FIG. 2. Displayed is the ordered magnetic moment obtained from the gap equation at $\Delta_0 = 740$ meV versus $t_2^\perp/i$, along with the corresponding on-site-orbital Hubbard U_0. The Hund's rule coupling is fixed at $J_0 = -100$ meV. Also, the square lattice of iron atoms is a periodic 1000×1000 grid. The remaining electron hopping parameters are listed in the caption to Fig. 1.

Here, $c_s^\dagger(1, \boldsymbol{k})$ and $c_s^\dagger(2, \boldsymbol{k})$ create plane waves (4) in the antibonding ($d_{y(\delta)z}$) and bonding ($d_{x(\delta)z}$) bands, respectively. Here also, intraband scattering has been neglected because it shows no nesting. After shifting the momentum of the antibonding band ($n = 1$) by $\boldsymbol{Q}_{\mathrm{AF}}$, we arrive at the final form of the mean-field Hamiltonian:

$$H^{(mf)} = \sum_s \sum_{\boldsymbol{k}} \varepsilon_+(\boldsymbol{k})[c_s^\dagger(2, \boldsymbol{k})c_s(2, \boldsymbol{k}) - c_s^\dagger(1, \bar{\boldsymbol{k}})c_s(1, \bar{\boldsymbol{k}})]$$
$$\mp \sum_s \sum_{\boldsymbol{k}} [(\mathrm{sgn}\, s)\Delta(\boldsymbol{k})c_s^\dagger(1, \bar{\boldsymbol{k}})c_s(2, \boldsymbol{k}) + \mathrm{H.c.}]. \tag{17}$$

For convenience, now set the $\pm$ sign that originates from the orbital matrix elements to minus. [See Appendix A and (31).] The mean-field Hamiltonian (17) is diagonalized in the usual way by writing the electron in terms of quasiparticle excitations [27–29]:

$$c_s^\dagger(2, \boldsymbol{k}) = u(\boldsymbol{k})\alpha_s^\dagger(2, \boldsymbol{k}) - (\mathrm{sgn}\, s)v(\boldsymbol{k})\alpha_s^\dagger(1, \bar{\boldsymbol{k}}),$$
$$c_s^\dagger(1, \bar{\boldsymbol{k}}) = (\mathrm{sgn}\, s)v(\boldsymbol{k})\alpha_s^\dagger(2, \boldsymbol{k}) + u(\boldsymbol{k})\alpha_s^\dagger(1, \bar{\boldsymbol{k}}). \tag{18}$$

Here, $u(\boldsymbol{k})$ and $v(\boldsymbol{k})$ are coherence factors with square magnitudes

$$u^2 = \frac{1}{2} + \frac{1}{2}\frac{\varepsilon_+}{E} \quad \text{and} \quad v^2 = \frac{1}{2} - \frac{1}{2}\frac{\varepsilon_+}{E}, \tag{19}$$

where $E(\boldsymbol{k}) = [\varepsilon_+^2(\boldsymbol{k}) + \Delta^2(\boldsymbol{k})]^{1/2}$. The mean-field Hamiltonian can then be expressed in terms of the occupation of quasiparticles as

$$H^{(mf)} = \sum_s \sum_{\boldsymbol{k}} E(\boldsymbol{k})[\alpha_s^\dagger(2, \boldsymbol{k})\alpha_s(2, \boldsymbol{k}) - \alpha_s^\dagger(1, \bar{\boldsymbol{k}})\alpha_s(1, \bar{\boldsymbol{k}})]. \tag{20}$$

The quasiparticle excitation energies are then $E(\boldsymbol{k})$ for particles and $E(\bar{\boldsymbol{k}})$ for holes, with a gap function (15) that has D_{xy} symmetry. Dirac nodes therefore emerge from the points on the Fermi surfaces indicated by Fig. 1. At half filling, the energy band $-E(\bar{\boldsymbol{k}})$ is filled and the energy band $+E(\boldsymbol{k})$ is empty. Last, inverting (18) yields

$$\alpha_s^\dagger(2, \boldsymbol{k}) = u(\boldsymbol{k})c_s^\dagger(2, \boldsymbol{k}) + (\mathrm{sgn}\, s)v(\boldsymbol{k})c_s^\dagger(1, \bar{\boldsymbol{k}}),$$
$$\alpha_s^\dagger(1, \bar{\boldsymbol{k}}) = -(\mathrm{sgn}\, s)v(\boldsymbol{k})c_s^\dagger(2, \boldsymbol{k}) + u(\boldsymbol{k})c_s^\dagger(1, \bar{\boldsymbol{k}}). \tag{21}$$

Quasiparticles are a coherent superposition of an electron of momentum $\boldsymbol{k}$ in the bonding ($+$) band 2 with an electron of momentum $\boldsymbol{k} + \boldsymbol{Q}_{\mathrm{AF}}$ in the antibonding ($-$) band 1.

Finally, to obtain the gap equation, we exploit the pattern of hidden Néel order (12), and write the gap maximum (16) as

$$\Delta_0 = \mathcal{N}^{-1} \sum_i \sum_\alpha U(\pi)\langle m_{i,\alpha}\rangle(-1)^\alpha e^{i\boldsymbol{Q}_{\mathrm{AF}}\cdot\boldsymbol{r}_i}$$
$$= \mathcal{N}^{-1} U(\pi)\langle S_z(\pi, \boldsymbol{Q}_{\mathrm{AF}})\rangle.$$

Using expressions for the hidden-order moment in terms of band states yields

$$\Delta_0 = -\mathcal{N}^{-1}\frac{1}{2} \sum_s \sum_{\boldsymbol{k}} \sum_n U(\pi)(\mathrm{sgn}\, s)$$
$$\times [\sin 2\delta(\boldsymbol{k})]\langle c_s^\dagger(\bar{n}, \bar{\boldsymbol{k}})c_s(n, \boldsymbol{k})\rangle,$$

where $\bar{n} = 1 + (n \bmod 2)$. [See Appendix A and (31).] Intraband scattering has again been neglected. Substituting in (18) and the conjugate annihilation operators, and recalling that the $n = 1$ quasiparticle band is filled, while the $n = 2$ quasiparticle band is empty, yields $\langle c_s^\dagger(\bar{n}, \bar{\boldsymbol{k}})c_s(n, \boldsymbol{k})\rangle =$
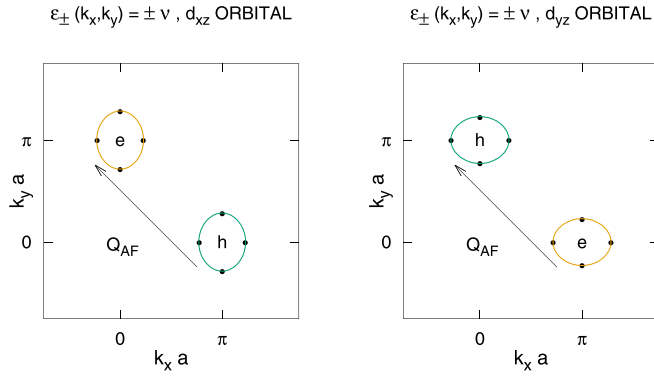
FIG. 3. Shown are the renormalized Fermi surface pockets after a Lifshitz transition due to fluctuation exchange with hidden spin waves centered at $\boldsymbol{Q}_{\mathrm{AF}}$. [See Ref. [19] and Eq. (62).] The orbital character is only approximate, although it becomes exact as the area of the Fermi surface pockets vanishes as U_0 diverges. Dirac cones emerge from the dots on the renormalized Fermi surfaces in the fluctuation-corrected hSDW state.

$-(\mathrm{sgn}\, s)u(\boldsymbol{k})v(\boldsymbol{k})$ for the expectation value. We thereby obtain

$$\Delta_0 = \mathcal{N}^{-1} \sum_{\boldsymbol{k}} U(\pi)[\sin 2\delta(\boldsymbol{k})]\Delta(\boldsymbol{k})/E(\boldsymbol{k}),$$

or equivalently, the gap equation

$$1 = U(\pi)\mathcal{N}^{-1} \sum_{\boldsymbol{k}} \frac{[\sin 2\delta(\boldsymbol{k})]^2}{\sqrt{\varepsilon_+^2(\boldsymbol{k}) + \Delta_0^2[\sin 2\delta(\boldsymbol{k})]^2}}. \qquad (22)$$

Figure 2 displays solutions of the gap equation at constant Δ_0. It is important to mention that they depend only on the hopping parameters and on $U(\pi)$. By (13), Δ_0 then is also constant along a line, U_0 versus $-J_0$, such that $U(\pi)$ remains constant.

B. Lifshitz transition of the Fermi surfaces

Before going on to the calculation of the dynamical spin susceptibility of the hSDW state within RPA in the next section, it is important to point out that ARPES on electron-doped iron selenide high-T_c superconductors generally sees only electron-type Fermi surface pockets at the corner of the folded (two-iron) Brillouin zone [13–16]. The perfectly nested Fermi surfaces displayed by Fig. 1 do *not*, therefore, coincide with ARPES measurements on these materials. The following RPA of the extended Hubbard model for electron-doped iron selenide reveals hidden spin waves (62) that disperse acoustically from the antiferromagnetic wave vector, $\boldsymbol{Q}_{\mathrm{AF}}$, however. In the critical hSDW state, as $\Delta_0 \to 0$, the author and a co-worker have recently shown that fluctuation-exchange interactions of the electrons with such Goldstone modes result in a Lifshitz transition of the nested Fermi surfaces displayed by [19] Fig. 1: the electron-type band $\varepsilon_+(\boldsymbol{k})$ is pulled down in energy with respect to the Fermi level, while the hole-type band $\varepsilon_-(\boldsymbol{k})$ is pulled up in energy by an equal and opposite amount. The Lifshitz transition results in electron/hole pockets near the opposite band edges at moderate to large Hubbard repulsion U_0. Figure 3 displays the resulting renormalized Fermi surfaces for hopping parameters that are listed in the caption to Fig. 1. Also, the above Lifshitz

transition is accompanied by wave function renormalizations that result in vanishingly small quasiparticle weight at the renormalized Fermi levels [19].

The Lifshitz transition described above was predicted at half filling for the critical hSDW state ($\Delta_0 \to 0$) via an Eliashberg-type theory of hidden spin-fluctuation exchange in the particle-hole channel [19]. The critical hSDW itself can be achieved by tuning the strength of Hund's rule to the transition point where a true SDW state appears. Adding electrons above half filling suggests a rigid shift up in energy of the Fermi level with respect to the renormalized band structure, $\varepsilon_+(\boldsymbol{k}) - \nu$ and $\varepsilon_-(\boldsymbol{k}) + \nu$. Here, $\nu > 0$ represents the energy shift due to the Lifshitz transition. It lies just below the upper band edge of the bonding (+) band. At saturation, a rigid shift in energy of such a renormalized band structure results in Fermi surface points for the new hole-type Fermi surfaces shown in Fig. 3, and in new electron-type Fermi surface pockets that are a bit larger than those shown in Fig. 3. Such a rigid energy shift has in fact been confirmed by the author in a related Eliashberg theory for hidden spin-fluctuation exchange, but in the conventional particle-particle channel [22]. In particular, the author finds that the quasiparticle weight of the holes remains vanishingly small at the Fermi level, while that of the quasiparticle weight of the electrons can be appreciable at the Fermi level. This scenario is confirmed by a local-moment model for the present extended Hubbard model that harbors the hSDW state [17].

In the following section, we will proceed to compute the dynamical spin susceptibility of the hSDW within RPA, but starting from the unrenormalized electron bands shown in Fig. 1. This is justified on the basis of perturbation theory in powers of the interactions, H_U and H_{sprx}. Does that conflict with the Lifshitz transition [19] shown by Fig. 3? We believe that is does not. By (7), the renormalized energy bands mentioned above trivially also satisfy perfect nesting:

$$\varepsilon_+(\boldsymbol{k} + \boldsymbol{Q}_{\mathrm{AF}}) - \nu = -[\varepsilon_-(\boldsymbol{k}) + \nu],$$
$$\varepsilon_-(\boldsymbol{k} + \boldsymbol{Q}_{\mathrm{AF}}) + \nu = -[\varepsilon_+(\boldsymbol{k}) - \nu]. \qquad (23)$$

The *form* of the RPA to be developed below does not therefore change if the shifted energy bands are used instead, along with the wave function renormalization. We therefore believe that starting the RPA below from the unrenormalized bands (Fig. 1) is compatible with the Lifshitz transition [19] mentioned above.

IV. SPIN FLUCTUATIONS WITHIN RANDOM PHASE APPROXIMATION

Is the previous mean-field solution for the hSDW state of the extended Hubbard model for electron-doped iron selenide [19] stable? To answer this question, we shall compute the transverse dynamical spin susceptibility within the random phase approximation. Like in the original "spin bag" calculation of the SDW state in the conventional Hubbard model over the square lattice [27], the bare dynamical spin susceptibilities (RPA bubbles) do not conserve crystal moment over the square lattice, whereas the interaction terms do. In the present case, additionally, the bare RPA bubbles also break orbital-swap symmetry, $P_{d,\bar{d}}$, because of orbital mixing ($t_2^\perp$), while the interaction terms preserve that symmetry as well.

A. Bare spin fluctuations at perfect nesting

We shall first compute the *bare* spin-fluctuation propagators in the hSDW state, at perfect nesting (7). Recall the spin-flip operator at relative momentum $\boldsymbol{q}$, in the true or hidden channel, $q_0 = 0$ or π:

$$S^+(q_0, \boldsymbol{q}) = \sum_i \sum_{\alpha=0,1} e^{iq_0\alpha} e^{i\boldsymbol{q}\cdot\boldsymbol{r}_i} c^\dagger_{i,\alpha,\uparrow} c_{i,\alpha,\downarrow}. \quad (24)$$

Here, the indices $\alpha = 0$ and 1 represent the $d-$ and $d+$ orbitals, respectively. In the band basis set by the plane-wave eigenstates (4) of the hopping Hamiltonian, it has the form

$$S^+(q_0, \boldsymbol{q}) = \sum_{\boldsymbol{k}} \sum_{n,n'} \mathcal{M}^{(q_0)}_{n,\boldsymbol{k};n',\boldsymbol{k}'} c^\dagger_\uparrow(n', \boldsymbol{k}') c_\downarrow(n, \boldsymbol{k}), \quad (25)$$

with $\boldsymbol{k}' = \boldsymbol{k} + \boldsymbol{q}$. Above, the indices $n = 1$ and 2 represent the antibonding and bonding bands that are in momentum-dependent orbitals $(-i)d_{y(\delta)z}$ and $d_{x(\delta)z}$, respectively. The orbital matrix element is computed in Appendix A, and it is given by

$$\mathcal{M}^{(m\pi)}_{n,\boldsymbol{k};n',\boldsymbol{k}'} = \begin{cases} \cos[\delta(\boldsymbol{k}) - \delta(\boldsymbol{k}')], & \text{for} \quad n' = n + m \pmod 2, \\ -i\sin[\delta(\boldsymbol{k}) - \delta(\boldsymbol{k}')], & \text{for} \quad n' = n + m + 1 \pmod 2. \end{cases} \quad (26)$$

Now define the Nambu-Gorkov spinor that incorporates the physics of nesting [19]:

$$C_s(\boldsymbol{k}) = \begin{bmatrix} c_s(2, \boldsymbol{k}) \\ c_s(1, \bar{\boldsymbol{k}}). \end{bmatrix} \quad (27)$$

The spin-flip operator (25) can then be broken up into four components by the 2×2 identity matrix, τ_0, and by the Pauli matrices, τ_1, τ_2, and τ_3:

$$S^+_\mu(q_0, \boldsymbol{q}) = \sum_{\boldsymbol{k}} \mathcal{M}^{(q_0)}_{\boldsymbol{k},\boldsymbol{k}'}(\mu) C^\dagger_\uparrow(\boldsymbol{k}') \tau_\mu C_\downarrow(\boldsymbol{k}), \quad (28)$$

with matrix elements

$$\mathcal{M}^{(0)}_{\boldsymbol{k},\boldsymbol{k}'}(\mu) = \begin{cases} \mathcal{M}^{(0)}_{1,\bar{\boldsymbol{k}};1,\bar{\boldsymbol{k}}'} = \cos[\delta(\boldsymbol{k}) - \delta(\boldsymbol{k}')] = \mathcal{M}^{(0)}_{2,\boldsymbol{k};2,\boldsymbol{k}'}, & \text{if } \mu = 0 \text{ (not nested)}, \\ i\mathcal{M}^{(0)}_{1,\bar{\boldsymbol{k}};2,\boldsymbol{k}'} = \pm\cos[\delta(\boldsymbol{k}) + \delta(\boldsymbol{k}')] = -i\mathcal{M}^{(0)}_{2,\boldsymbol{k};1,\bar{\boldsymbol{k}}'}, & \text{if } \mu = 2 \text{ (nested)}, \\ 0, & \text{if } \mu = 1, 3, \end{cases} \quad (29)$$

and

$$\mathcal{M}^{(\pi)}_{\boldsymbol{k},\boldsymbol{k}'}(\mu) = \begin{cases} -\mathcal{M}^{(\pi)}_{1,\bar{\boldsymbol{k}};1,\bar{\boldsymbol{k}}'} = -i\sin[\delta(\boldsymbol{k}) - \delta(\boldsymbol{k}')] = \mathcal{M}^{(\pi)}_{2,\boldsymbol{k};2,\boldsymbol{k}'}, & \text{if } \mu = 3 \text{ (not nested)}, \\ \mathcal{M}^{(\pi)}_{1,\bar{\boldsymbol{k}};2,\boldsymbol{k}'} = \pm\sin[\delta(\boldsymbol{k}) + \delta(\boldsymbol{k}')] = \mathcal{M}^{(\pi)}_{2,\boldsymbol{k};1,\bar{\boldsymbol{k}}'}, & \text{if } \mu = 1 \text{ (nested)}, \\ 0, & \text{if } \mu = 0, 2. \end{cases} \quad (30)$$

Here, we have used the property

$$\delta(\boldsymbol{k} + \boldsymbol{Q}_{\text{AF}}) = \pm\frac{\pi}{2} - \delta(\boldsymbol{k}) \quad (31)$$

satisfied by the phase shift, which is a result of the property $\varepsilon_\perp(\boldsymbol{k} + \boldsymbol{Q}_{\text{AF}}) = -\varepsilon_\perp^*(\boldsymbol{k})$ satisfied by the matrix element (5b). The components $S^+_\mu(q_0, \boldsymbol{q})$ of the spin-flip operator (24) can then be reassembled following the nesting (1) versus the non-nesting (0) nature of the momentum transfer, $\boldsymbol{q}$:

$$S^+_{q_0,0}(\boldsymbol{q}) = S^+_0(q_0, \boldsymbol{q}) + S^+_3(q_0, \boldsymbol{q}) \quad \text{(not nested)},$$
$$S^+_{q_0,1}(\boldsymbol{q}) = S^+_1(q_0, \boldsymbol{q}) + S^+_2(q_0, \boldsymbol{q}) \quad \text{(nested)}. \quad (32)$$

Inspection of (29) and (30) then yields that the above spin operators take the form

$$S^+_{q_0,\gamma}(\boldsymbol{q}) = \sum_{\boldsymbol{k}} \mathcal{M}^{(q_0,\gamma)}_{\boldsymbol{k},\boldsymbol{k}'} C^\dagger_\uparrow(\boldsymbol{k}') \tau_{(q_0,\gamma)} C_\downarrow(\boldsymbol{k}), \quad (33)$$

where the products $\mathcal{M}^{(q_0,\gamma)}_{\boldsymbol{k},\boldsymbol{k}'} \tau_{(q_0,\gamma)}$ are listed in Table III.

Next, en route to computing the bare spin-fluctuation propagator of the hSDW state within mean-field theory, we will first compute the Nambu-Gorkov Green's function. Let $C_s(\boldsymbol{k}, t)$ denote the time evolution of the destruction operators (27) $C_s(\boldsymbol{k})$, and let $C^\dagger_s(\boldsymbol{k}, t)$ denote the time evolution of the conjugate creation operators $C^\dagger_s(\boldsymbol{k})$. The Nambu-Gorkov electron propagator is then the Fourier transform $iG_s(\boldsymbol{k}, \omega) = \int dt_{1,2} e^{i\omega t_{1,2}} \langle T[C_s(\boldsymbol{k}, t_1) C^\dagger_s(\boldsymbol{k}, t_2)] \rangle$, where $t_{1,2} = t_1 - t_2$, and where T is the time-ordering operator. It is a 2×2 matrix. By expression (17) for the mean-field Hamiltonian, the matrix inverse of the Nambu-Gorkov Green's function takes the form

$$G_s^{-1}(\boldsymbol{k}, \omega) = \omega\,\tau_0 - \varepsilon_+(\boldsymbol{k})\,\tau_3 \pm (\text{sgn}\, s)\Delta(\boldsymbol{k})\,\tau_1. \quad (34)$$

Here, $\Delta(\boldsymbol{k})$ is the quasiparticle gap (15). Notice that the term proportional to τ_3 is a direct consequence of perfect nesting (7). Matrix inversion of (34) yields the Nambu-Gorkov

TABLE III. The products $\mathcal{M}^{(q_0,\gamma)}_{\boldsymbol{k},\boldsymbol{k}'} \tau_{(q_0,\gamma)}$ that appear in $S^+_{q_0,\gamma}(\boldsymbol{q})$, where $q_0 = 0, \pi$ are labels for true versus hidden spin, and where $\gamma = 0, 1$ are labels for un-nested versus nested momentum transfer. [See Eqs. (25)–(33).]

	Not nested (0)	Nested (1)
True spin (0)	$\cos[\delta(\boldsymbol{k}) - \delta(\boldsymbol{k}')]\tau_0$	$\pm\cos[\delta(\boldsymbol{k}) + \delta(\boldsymbol{k}')]\tau_2$
Hidden spin (π)	$-i\sin[\delta(\boldsymbol{k}) - \delta(\boldsymbol{k}')]\tau_3$	$\pm\sin[\delta(\boldsymbol{k}) + \delta(\boldsymbol{k}')]\tau_1$

Green's function [19,23–25] $G = \sum_{\mu=0}^{3} G^{(\mu)}\tau_{\mu}$, with components

$$G_s^{(0)} = \frac{1}{2}\left(\frac{1}{\omega - E} + \frac{1}{\omega + E}\right),$$

$$G_s^{(1)} = \mp\frac{1}{2}\left(\frac{1}{\omega - E} - \frac{1}{\omega + E}\right)\frac{\Delta}{E}(\text{sgn }s),$$

$$G_s^{(2)} = 0,$$

$$G_s^{(3)} = \frac{1}{2}\left(\frac{1}{\omega - E} - \frac{1}{\omega + E}\right)\frac{\varepsilon_+}{E}. \tag{35}$$

Above, the excitation energy is $E = (\varepsilon_+^2 + \Delta^2)^{1/2}$.

We shall now define the bare dynamical spin susceptibility of the hSDW state with indices composed of true/hidden spin (q_0) and of un-nested/nested momentum transfer (γ):

$$\chi_{q_0,\gamma;q_0',\gamma'}^{(0)+-}(\boldsymbol{q}, \omega) = \frac{i}{\mathcal{N}}\langle S_{q_0,\gamma}^+(\boldsymbol{q}, \omega)S_{q_0',\gamma'}^-(\boldsymbol{q}, \omega)\rangle. \tag{36}$$

Here, $S_{q_0,\gamma}^+(\boldsymbol{q}, \omega)$ is the Fourier transform of the time-evolution of the spin-flip operator, $S_{q_0,\gamma}^+(\boldsymbol{q})$. [See (32) and (33).] Analytically continuing this dynamical spin susceptibility to imaginary time yields a convolution in terms of Matsubara frequencies:

$$\chi_{q_0,\gamma;q_0',\gamma'}^{(0)+-}(\boldsymbol{q}, i\omega_m) = \frac{k_B T}{\mathcal{N}} \sum_{i\omega_n} \sum_{\boldsymbol{k}} \text{tr}\big[G_\uparrow(\boldsymbol{k}', i\omega_{n'})\tau_{(q_0,\gamma)}$$
$$\times G_\downarrow(\boldsymbol{k}, i\omega_n)\tau_{(q_0',\gamma')}\big]\mathcal{M}_{\boldsymbol{k},\boldsymbol{k}'}^{(q_0,\gamma)}\mathcal{M}_{\boldsymbol{k},\boldsymbol{k}'}^{(q_0',\gamma')*}, \tag{37}$$

where the orbital matrix element $\mathcal{M}_{\boldsymbol{k},\boldsymbol{k}'}^{(q_0,\gamma)}$ appears as a product with the 2×2 matrix $\tau_{(q_0,\gamma)}$ in Table III. Here, $\boldsymbol{k}' = \boldsymbol{k} + \boldsymbol{q}$ and $i\omega_{n'} = i\omega_n + i\omega_m$. Substituting in the Nambu-Gorkov Green's function (35) yields the expression

$$\chi_{p_0,\gamma;q_0,\delta}^{(0)+-}(\boldsymbol{q}, i\omega_m) = \frac{k_B T}{\mathcal{N}} \sum_{i\omega_n} \sum_{\boldsymbol{k}} \sum_{\mu,\nu=0}^{3} \text{tr}\big[\tau_\mu \tau_{(p_0,\gamma)}\tau_\nu \tau_{(q_0,\delta)}\big]G_\uparrow^{(\mu)}(\boldsymbol{k}', i\omega_{n'})G_\downarrow^{(\nu)}(\boldsymbol{k}, i\omega_n)\mathcal{M}_{\boldsymbol{k},\boldsymbol{k}'}^{(p_0,\gamma)}\mathcal{M}_{\boldsymbol{k},\boldsymbol{k}'}^{(q_0,\delta)*} \tag{38}$$

for the bare dynamical spin susceptibility.

It is well known that the sum over Matsubara frequencies in the expression above for the bare dynamical spin susceptibility (38) can be evaluated in terms of Fermi-Dirac distribution functions. Below, we obtain the corresponding Lindhard functions in the zero-temperature limit. The required trace formulas for products of 2×2 matrices are listed in Appendix B.

(1) (0, 0; 0, 0): true spin; true spin. $\mathcal{M}_{\boldsymbol{k},\boldsymbol{k}'}^{(0,0)}\mathcal{M}_{\boldsymbol{k},\boldsymbol{k}'}^{(0,0)*} = \cos^2(\delta - \delta')$ and $\text{tr}(\tau_\mu\tau_0\tau_\nu\tau_0) = 2\delta_{\mu,\nu}$. Then

$$\sum_{\mu,\nu=0}^{3} \text{tr}(\tau_\mu\tau_0\tau_\nu\tau_0)G_\uparrow^{\prime(\mu)}G_\downarrow^{(\nu)} = 2[G_\uparrow^{\prime(0)}G_\downarrow^{(0)} + G_\uparrow^{\prime(1)}G_\downarrow^{(1)} + G_\uparrow^{\prime(3)}G_\downarrow^{(3)}].$$

Hence,

$$\chi_{0,0;0,0}^{(0)+-}(\boldsymbol{q}, \omega) = \frac{1}{2\mathcal{N}} \sum_{\boldsymbol{k}}\left(1 - \frac{\varepsilon_+\varepsilon_+' - \Delta\Delta'}{EE'}\right)\left(\frac{1}{E + E' - \omega} + \frac{1}{E + E' + \omega}\right)$$
$$\times \frac{1}{2}[1 + (\cos 2\delta)(\cos 2\delta') + (\sin 2\delta)(\sin 2\delta')]. \tag{39}$$

(2) (0, 0; π, 0): true spin; hidden spin. $\mathcal{M}_{\boldsymbol{k},\boldsymbol{k}'}^{(0,0)}\mathcal{M}_{\boldsymbol{k},\boldsymbol{k}'}^{(\pi,0)*} = i\cos(\delta - \delta')\sin(\delta - \delta')$ and $\text{tr}(\tau_\mu\tau_0\tau_\nu\tau_3) = 2(\delta_{\mu,0}\delta_{\nu,3} + \delta_{\mu,3}\delta_{\nu,0} + i\epsilon_{\mu,\nu,3})$, where $\epsilon_{\mu,\nu,i}$ coincides with the Levi-Civita tensor for $\mu, \nu = 1, 2, 3$, while it vanishes otherwise, for $\mu = 0$, or for $\nu = 0$. Then

$$\sum_{\mu,\nu=0}^{3} \text{tr}(\tau_\mu\tau_0\tau_\nu\tau_3)G_\uparrow^{\prime(\mu)}G_\downarrow^{(\nu)} = 2[G_\uparrow^{\prime(0)}G_\downarrow^{(3)} + G_\uparrow^{\prime(3)}G_\downarrow^{(0)}].$$

Hence,

$$\chi_{0,0;\pi,0}^{(0)+-}(\boldsymbol{q}, \omega) = -\frac{1}{2\mathcal{N}} \sum_{\boldsymbol{k}}\left(\frac{\varepsilon_+}{E} - \frac{\varepsilon_+'}{E'}\right)\left(\frac{1}{E + E' - \omega} - \frac{1}{E + E' + \omega}\right)\frac{i}{2}[(\sin 2\delta)(\cos 2\delta') - (\cos 2\delta)(\sin 2\delta')]. \tag{40}$$

(3) (0, 0; 0, 1): true spin; SDW moment. $\mathcal{M}_{\boldsymbol{k},\boldsymbol{k}'}^{(0,0)}\mathcal{M}_{\boldsymbol{k},\boldsymbol{k}'}^{(0,1)*} = \pm\cos(\delta - \delta')\cos(\delta + \delta')$ and $\text{tr}(\tau_\mu\tau_0\tau_\nu\tau_2) = 2(\delta_{\mu,0}\delta_{\nu,2} + \delta_{\mu,2}\delta_{\nu,0} + i\epsilon_{\mu,\nu,2})$. Then

$$\sum_{\mu,\nu=0}^{3} \text{tr}(\tau_\mu\tau_0\tau_\nu\tau_3)G_\uparrow^{\prime(\mu)}G_\downarrow^{(\nu)} = 2i[G_\uparrow^{\prime(3)}G_\downarrow^{(1)} - G_\uparrow^{\prime(1)}G_\downarrow^{(3)}].$$

Hence,

$$\chi_{0,0;0,1}^{(0)+-}(\boldsymbol{q}, \omega) = -\frac{1}{2\mathcal{N}} \sum_{\boldsymbol{k}} \frac{\varepsilon_+\Delta' + \Delta\varepsilon_+'}{EE'}\left(\frac{1}{E + E' - \omega} + \frac{1}{E + E' + \omega}\right)\frac{i}{2}[(\cos 2\delta) + (\cos 2\delta')]. \tag{41}$$

(4) $(0, 0; \pi, 1)$: true spin; hSDW moment. $\mathcal{M}_{\boldsymbol{k},\boldsymbol{k}'}^{(0,0)} \mathcal{M}_{\boldsymbol{k},\boldsymbol{k}'}^{(\pi,1)*} = \pm \cos(\delta - \delta') \sin(\delta + \delta')$ and $\mathrm{tr}(\tau_\mu \tau_0 \tau_\nu \tau_1) = 2(\delta_{\mu,0}\delta_{\nu,1} + \delta_{\mu,1}\delta_{\nu,0} + i\epsilon_{\mu,\nu,1})$.
Then

$$\sum_{\mu,\nu=0}^{3} \mathrm{tr}(\tau_\mu \tau_0 \tau_\nu \tau_1) G_\uparrow^{\prime(\mu)} G_\downarrow^{(\nu)} = 2[G_\uparrow^{\prime(0)} G_\downarrow^{(1)} + G_\uparrow^{\prime(1)} G_\downarrow^{(0)}].$$

Hence,

$$\chi_{0,0;\pi,1}^{(0)+-}(\boldsymbol{q}, \omega) = -\frac{1}{2\mathcal{N}} \sum_{\boldsymbol{k}} \left(\frac{\Delta}{E} + \frac{\Delta'}{E'} \right) \left(\frac{1}{E + E' - \omega} - \frac{1}{E + E' + \omega} \right) \frac{1}{2}[(\sin 2\delta) + (\sin 2\delta')]. \tag{42}$$

(5) $(\pi, 0; \pi, 0)$: hidden spin; hidden spin. $\mathcal{M}_{\boldsymbol{k},\boldsymbol{k}'}^{(\pi,0)} \mathcal{M}_{\boldsymbol{k},\boldsymbol{k}'}^{(\pi,0)*} = \sin^2(\delta - \delta')$ and $\mathrm{tr}(\tau_\mu \tau_3 \tau_\nu \tau_3) = 2\,\mathrm{sgn}_\mu(3)\delta_{\mu,\nu}$, where $\mathrm{sgn}_\mu(i) = 1$ if $\mu = 0$ or i, and where $\mathrm{sgn}_\mu(i) = -1$ otherwise. Then

$$\sum_{\mu,\nu=0}^{3} \mathrm{tr}(\tau_\mu \tau_3 \tau_\nu \tau_3) G_\uparrow^{\prime(\mu)} G_\downarrow^{(\nu)} = 2[G_\uparrow^{\prime(0)} G_\downarrow^{(0)} - G_\uparrow^{\prime(1)} G_\downarrow^{(1)} + G_\uparrow^{\prime(3)} G_\downarrow^{(3)}].$$

Hence,

$$\chi_{\pi,0;\pi,0}^{(0)+-}(\boldsymbol{q}, \omega) = \frac{1}{2\mathcal{N}} \sum_{\boldsymbol{k}} \left(1 - \frac{\varepsilon_+ \varepsilon_+' + \Delta\Delta'}{EE'} \right) \left(\frac{1}{E + E' - \omega} + \frac{1}{E + E' + \omega} \right)$$
$$\times \frac{1}{2}[1 - (\cos 2\delta)(\cos 2\delta') - (\sin 2\delta)(\sin 2\delta')]. \tag{43}$$

(6) $(\pi, 0; 0, 1)$: hidden spin; SDW moment. $\mathcal{M}_{\boldsymbol{k},\boldsymbol{k}'}^{(\pi,0)} \mathcal{M}_{\boldsymbol{k},\boldsymbol{k}'}^{(0,1)*} = \mp i \sin(\delta - \delta') \cos(\delta + \delta')$ and $\mathrm{tr}(\tau_\mu \tau_3 \tau_\nu \tau_2) = 2(\delta_{\mu,3}\delta_{\nu,2} + \delta_{\mu,2}\delta_{\nu,3} + i\delta_{\mu,0}\epsilon_{3,\nu,2} + i\delta_{\nu,0}\epsilon_{\mu,3,2})$. Then

$$\sum_{\mu,\nu=0}^{3} \mathrm{tr}(\tau_\mu \tau_3 \tau_\nu \tau_2) G_\uparrow^{\prime(\mu)} G_\downarrow^{(\nu)} = 2i[G_\uparrow^{\prime(0)} G_\downarrow^{(1)} - G_\uparrow^{\prime(1)} G_\downarrow^{(0)}].$$

Hence,

$$\chi_{\pi,0;0,1}^{(0)+-}(\boldsymbol{q}, \omega) = -\frac{1}{2\mathcal{N}} \sum_{\boldsymbol{k}} \left(\frac{\Delta}{E} - \frac{\Delta'}{E'} \right) \left(\frac{1}{E + E' - \omega} - \frac{1}{E + E' + \omega} \right) \frac{1}{2}[(\sin 2\delta) - (\sin 2\delta')]. \tag{44}$$

(7) $(\pi, 0; \pi, 1)$: hidden spin; hSDW moment. $\mathcal{M}_{\boldsymbol{k},\boldsymbol{k}'}^{(\pi,0)} \mathcal{M}_{\boldsymbol{k},\boldsymbol{k}'}^{(\pi,1)*} = \mp i \sin(\delta - \delta') \sin(\delta + \delta')$ and $\mathrm{tr}(\tau_\mu \tau_3 \tau_\nu \tau_1) = 2(\delta_{\mu,3}\delta_{\nu,1} + \delta_{\mu,1}\delta_{\nu,3} + i\delta_{\mu,0}\epsilon_{3,\nu,1} + i\delta_{\nu,0}\epsilon_{\mu,3,1})$. Then

$$\sum_{\mu,\nu=0}^{3} \mathrm{tr}(\tau_\mu \tau_3 \tau_\nu \tau_1) G_\uparrow^{\prime(\mu)} G_\downarrow^{(\nu)} = 2[G_\uparrow^{\prime(3)} G_\downarrow^{(1)} + G_\uparrow^{\prime(1)} G_\downarrow^{(3)}].$$

Hence,

$$\chi_{\pi,0;\pi,1}^{(0)+-}(\boldsymbol{q}, \omega) = \frac{1}{2\mathcal{N}} \sum_{\boldsymbol{k}} \frac{\varepsilon_+ \Delta' - \Delta \varepsilon_+'}{EE'} \left(\frac{1}{E + E' - \omega} + \frac{1}{E + E' + \omega} \right) \frac{i}{2}[(\cos 2\delta) - (\cos 2\delta')]. \tag{45}$$

(8) $(0, 1; 0, 1)$: SDW moment; SDW moment. $\mathcal{M}_{\boldsymbol{k},\boldsymbol{k}'}^{(0,1)} \mathcal{M}_{\boldsymbol{k},\boldsymbol{k}'}^{(0,1)*} = \cos^2(\delta + \delta')$ and $\mathrm{tr}(\tau_\mu \tau_2 \tau_\nu \tau_2) = 2\,\mathrm{sgn}_\mu(2)\delta_{\mu,\nu}$. Then

$$\sum_{\mu,\nu=0}^{3} \mathrm{tr}(\tau_\mu \tau_2 \tau_\nu \tau_2) G_\uparrow^{\prime(\mu)} G_\downarrow^{(\nu)} = 2[G_\uparrow^{\prime(0)} G_\downarrow^{(0)} - G_\uparrow^{\prime(1)} G_\downarrow^{(1)} - G_\uparrow^{\prime(3)} G_\downarrow^{(3)}].$$

Hence,

$$\chi_{0,1;0,1}^{(0)+-}(\boldsymbol{q}, \omega) = \frac{1}{2\mathcal{N}} \sum_{\boldsymbol{k}} \left(1 + \frac{\varepsilon_+ \varepsilon_+' - \Delta\Delta'}{EE'} \right) \left(\frac{1}{E + E' - \omega} + \frac{1}{E + E' + \omega} \right)$$
$$\times \frac{1}{2}[1 + (\cos 2\delta)(\cos 2\delta') - (\sin 2\delta)(\sin 2\delta')]. \tag{46}$$

(9) $(0, 1; \pi, 1)$: SDW moment; hSDW moment. $\mathcal{M}_{k,k'}^{(0,1)} \mathcal{M}_{k,k'}^{(\pi,1)*} = \cos(\delta + \delta') \sin(\delta + \delta')$ and $\text{tr}(\tau_\mu \tau_2 \tau_\nu \tau_1) = 2(\delta_{\mu,2}\delta_{\nu,1} + \delta_{\mu,1}\delta_{\nu,2} + i\delta_{\mu,0}\epsilon_{2,\nu,1} + i\delta_{\nu,0}\epsilon_{\mu,2,1})$. Then

$$\sum_{\mu,\nu=0}^{3} \text{tr}(\tau_\mu \tau_2 \tau_\nu \tau_1) G_\uparrow^{\prime(\mu)} G_\downarrow^{(\nu)} = 2i[G_\uparrow^{\prime(0)} G_\downarrow^{(3)} - G_\uparrow^{\prime(3)} G_\downarrow^{(0)}].$$

Hence,

$$\chi_{0,1;\pi,1}^{(0)+-}(\boldsymbol{q}, \omega) = -\frac{1}{2\mathcal{N}} \sum_k \left(\frac{\varepsilon_+}{E} + \frac{\varepsilon_+'}{E'} \right) \left(\frac{1}{E + E' - \omega} - \frac{1}{E + E' + \omega} \right) \frac{i}{2} [(\sin 2\delta)(\cos 2\delta') + (\cos 2\delta)(\sin 2\delta')]. \quad (47)$$

(10) $(\pi, 1; \pi, 1)$: hSDW moment; hSDW moment. $\mathcal{M}_{k,k'}^{(\pi,1)} \mathcal{M}_{k,k'}^{(\pi,1)*} = \sin^2(\delta + \delta')$ and $\text{tr}(\tau_\mu \tau_1 \tau_\nu \tau_1) = 2\,\text{sgn}_\mu(1)\delta_{\mu,\nu}$. Then

$$\sum_{\mu,\nu=0}^{3} \text{tr}(\tau_\mu \tau_1 \tau_\nu \tau_1) G_\uparrow^{\prime(\mu)} G_\downarrow^{(\nu)} = 2[G_\uparrow^{\prime(0)} G_\downarrow^{(0)} + G_\uparrow^{\prime(1)} G_\downarrow^{(1)} - G_\uparrow^{\prime(3)} G_\downarrow^{(3)}].$$

Hence,

$$\chi_{\pi,1;\pi,1}^{(0)+-}(\boldsymbol{q}, \omega) = \frac{1}{2\mathcal{N}} \sum_k \left(1 + \frac{\varepsilon_+ \varepsilon_+' + \Delta\Delta'}{EE'} \right) \left(\frac{1}{E + E' - \omega} + \frac{1}{E + E' + \omega} \right) \frac{1}{2}[1 - (\cos 2\delta)(\cos 2\delta') + (\sin 2\delta)(\sin 2\delta')].$$

$$(48)$$

Last, inspection of the trace formulas for products of 2×2 matrices listed in Appendix B yields that the matrix formed by the trace $\text{tr}(\tau_\mu \tau_\gamma \tau_\nu \tau_\delta)$ as a function of the indices γ and δ is Hermitian. The matrix of bare spin susceptibilities is then also Hermitian by expression (38). The remaining off-diagonal bare spin susceptibilities are then complex conjugates of those listed above.

B. Random phase approximation

Next, to construct the RPA, we must determine how the interaction terms in H_U (8) and in H_{sprx} (9) couple to the previous bare dynamical spin susceptibilities. All of the interaction terms are translationally invariant. They are also all invariant under orbital swap, $P_{d,\bar{d}}$: $d\pm \to d\mp$. Both momentum and parity, $\boldsymbol{q}$ and q_0, are then good quantum numbers for the interactions H_U and H_{sprx}. They are therefore diagonal in momentum and in parity. Yet what are such diagonal matrix elements of H_U and of H_{sprx}?

The on-site-orbital Hubbard repulsion (U_0) has the form $n_\uparrow n_\downarrow = +c_\uparrow^\dagger c_\downarrow^\dagger c_\downarrow c_\uparrow$. On the other hand, the spin-flip part of the on-site Hund's rule coupling (J_0) and of the superexchange interactions (J_1 and J_2) have the transverse Heisenberg-exchange form

$$\tfrac{1}{2}S^+S'^- + \tfrac{1}{2}S^-S'^+ = -\tfrac{1}{2}c_\uparrow^\dagger c_\downarrow'^\dagger c_\downarrow c_\uparrow' - \tfrac{1}{2}c_\downarrow^\dagger c_\uparrow'^\dagger c_\uparrow c_\downarrow'.$$

Figure 4 displays the corresponding Feynman diagrams for the RPA. Taking the Fourier transform of the previous interactions in site-orbital space yields the following spin-flip contribution to the interaction:

$$V^{+-}(q_0, \boldsymbol{q}) = U_0 - \tfrac{1}{2}J_0 \cos(q_0)$$
$$- \delta_{q_0,0}\{2J_1[\cos(q_x a) + \cos(q_y a)]$$
$$+ 2J_2[\cos(q_+ a) + \cos(q_- a)]\}. \quad (49)$$

Here, $q_\pm = q_x \pm q_y$. Last, interorbital on-site interactions (U_0') can be neglected because they couple only to density, while on-site Josephson tunneling (J_0') can be neglected at strong on-site repulsion U_0.

The true-spin and the hidden-spin components of the spin-flip potential $V^{+-}(q_0, \boldsymbol{q})$ are listed in the first-two rows of Table IV. They clearly scatter fermions at un-nested momentum transfer, $\boldsymbol{q}$ small. The last two rows in Table IV, however, are the corresponding spin-flip interaction potentials that scatter fermions at momentum transfer that is indeed nested, $\boldsymbol{q}$ small. These are simply shifted with respect to the former un-nested spin-flip potentials by the antiferromagnetic wave vector $\boldsymbol{Q}_{\text{AF}} = (\pi/a, \pi/a)$. Adding up the Dyson series of Feynman diagrams of the types displayed by Fig. 4 yields the RPA for the dynamical spin susceptibility:

$$\chi^{+-}(\boldsymbol{q}, \omega) = \chi^{(0)+-}(\boldsymbol{q}, \omega)[1 - V^{+-}(\boldsymbol{q})\chi^{(0)+-}(\boldsymbol{q}, \omega)]^{-1}.$$
$$(50)$$

Above, $V^{+-}(\boldsymbol{q})$ is a 4×4 matrix with diagonal matrix elements that are listed in Table IV, and with off-diagonal matrix elements that are null. The matrix elements of the bare
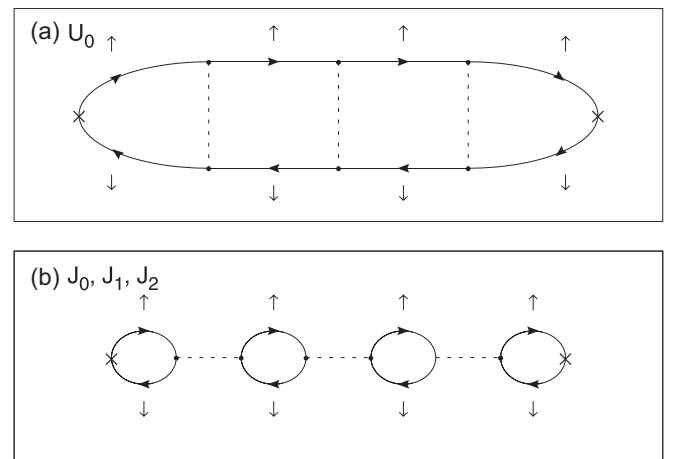

FIG. 4. Representative Feynman diagrams for the dynamical transverse spin susceptibility, $\chi^{+-}(\boldsymbol{q}, \omega)$, of the extended two-orbital Hubbard model within RPA.

TABLE IV. Interactions in momentum space per true (0) and hidden (π) spin quantum numbers. The SDW and hSWD interactions are the nested versions of the previous; i.e., $q \to q + Q_{AF}$.

(q_0, γ)	$V_{q_0,\gamma}^{+-}(q)$
True spin $(0, 0)$	$U_0 - \frac{1}{2}J_0 - 2J_1[\cos(q_x a) + \cos(q_y a)] - 2J_2[\cos(q_+ a) + \cos(q_- a)]$
Hidden spin $(\pi, 0)$	$U_0 + \frac{1}{2}J_0$
SDW moment $(0, 1)$	$U_0 - \frac{1}{2}J_0 + 2J_1[\cos(q_x a) + \cos(q_y a)] - 2J_2[\cos(q_+ a) + \cos(q_- a)]$
hSDW moment $(\pi, 1)$	$U_0 + \frac{1}{2}J_0$

dynamical spin susceptibility, $\chi^{(0)+-}(q, \omega)$, are listed above in the previous subsection.

C. Reflection symmetries and the long-wavelength limit

In general, the bare dynamical spin susceptibility, $\chi^{(0)+-}(q, \omega)$, is a dense 4×4 matrix. It and the RPA solution (50) break down into block-diagonal 2×2 matrices at momentum transfers that are along a principal axis of the first Brillouin zone, however. To demonstrate this, suppose that the momentum transfer q lies (i) along one of the horizontal or vertical principal axes of the Brillouin zone shown by Fig. 5. Reflections about such principal axes act on momenta as

$$R_x : (k_x, k_y) \to (k_x, -k_y),$$
$$R_y : (k_x, k_y) \to (-k_x, k_y). \tag{51}$$

Inspection of expressions (6a) and (6b) then yields that the components of the orbital phase factor transform under such reflections as

$$R_{x(y)} : (\cos 2\delta, \sin 2\delta) \to (\cos 2\delta, -\sin 2\delta). \tag{52}$$

Next, suppose instead that the momentum transfer q lies (ii) along one of the diagonal principal axes of the Brillouin zone shown by Fig. 5. Reflections about such principal axes act on
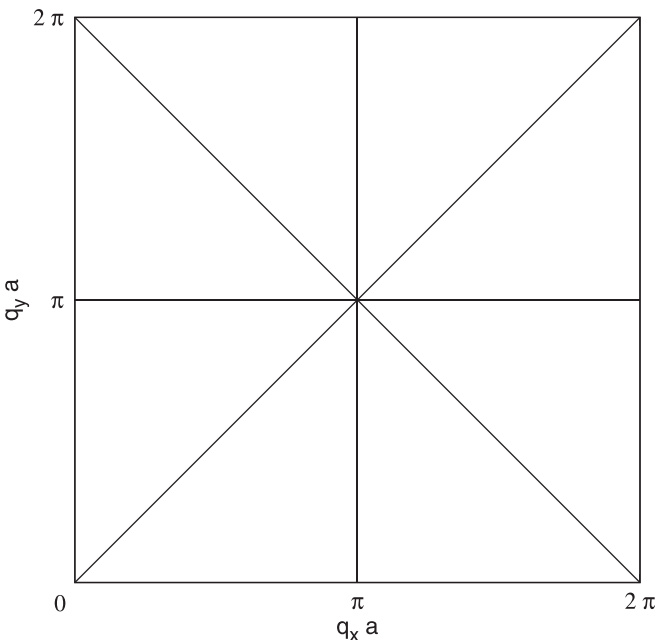

FIG. 5. Principal axes in the first Brillouin zone.

momenta as

$$R_{x'} : (k_x, k_y) \to (k_y, k_x),$$
$$R_{y'} : (k_x, k_y) \to (-k_y, -k_x), \tag{53}$$

on the other hand. Inspection of expressions (6a) and (6b) then yields that the components of the orbital phase factor transform under such reflections as

$$R_{x'(y')} : (\cos 2\delta, \sin 2\delta) \to (-\cos 2\delta, \sin 2\delta). \tag{54}$$

Observe, now, that the energy eigenvalue $\varepsilon_+(k)$ is invariant under all such reflections about a principal axis. Inspection of the integrands of the bare dynamical spin susceptibilities, $\chi_{p_0,\gamma;q_0,\delta}^{(0)+-}(q, \omega)$, listed above then yields unique parities under all such reflections for q along the reflection axis. They are listed in Table V. We thereby conclude that the off-diagonal components of the bare dynamical spin susceptibility with negative parities are *null* for momentum transfer q along a principal axis.

At momentum transfer q along a principal axis, the RPA solution (50) for the dynamical spin susceptibility therefore decouples into two 2×2 blocks among the pairs of components (1,4) and (2,3):

$$\begin{bmatrix} \chi_{11}^{+-} & \chi_{14}^{+-} \\ \chi_{41}^{+-} & \chi_{44}^{+-} \end{bmatrix} = \frac{1}{d(1,4)} \begin{bmatrix} \chi_{11}^{(0)+-} & \chi_{14}^{(0)+-} \\ \chi_{41}^{(0)+-} & \chi_{44}^{(0)+-} \end{bmatrix}$$
$$\times \begin{bmatrix} 1 - V_4^{+-}\chi_{44}^{(0)+-} & +V_1^{+-}\chi_{14}^{(0)+-} \\ +V_4^{+-}\chi_{41}^{(0)+-} & 1 - V_1^{+-}\chi_{11}^{(0)+-} \end{bmatrix}, \tag{55}$$

with determinant

$$d(1,4) = \left(1 - V_1^{+-}\chi_{11}^{(0)+-}\right)\left(1 - V_4^{+-}\chi_{44}^{(0)+-}\right)$$
$$- V_1^{+-}V_4^{+-}\chi_{14}^{(0)+-}\chi_{41}^{(0)+-}, \tag{56}$$

TABLE V. Parities of the integrands of the bare dynamical spin susceptibility, $\chi_{p_0,\gamma;q_0,\delta}^{(0)+-}(q, \omega)$, under reflection, R, about a principal axis of the Brillouin zone, at momentum transfers, q, along the same axis. (See Fig. 5.)

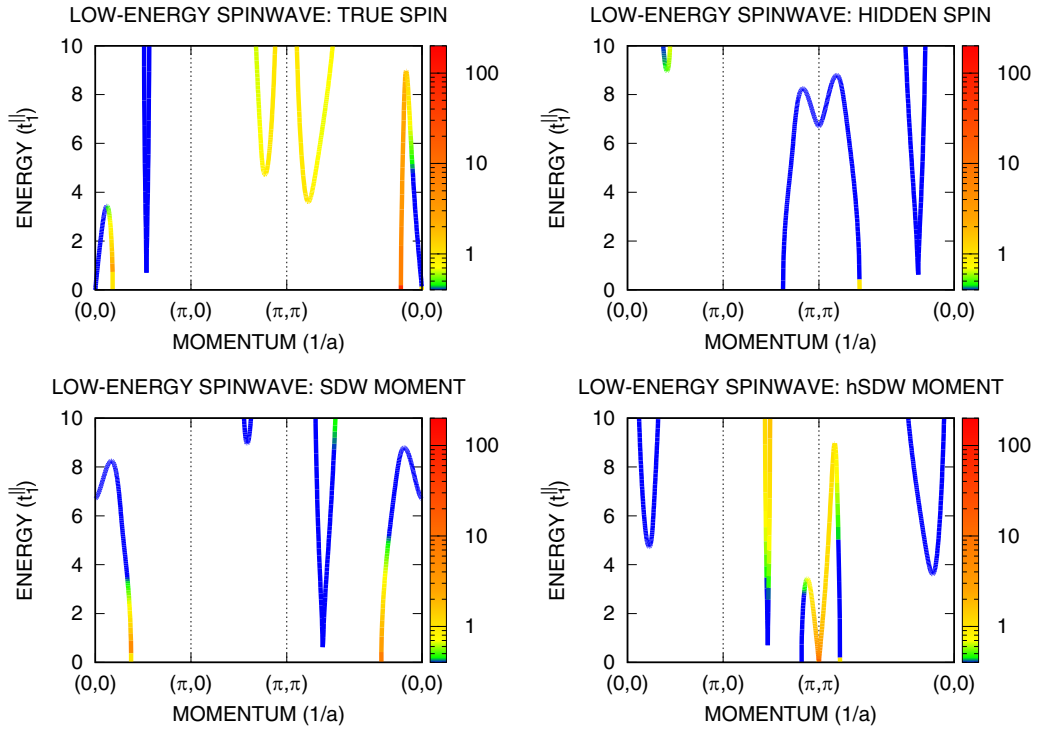| R	$0, 0$	$\pi, 0$	$0, 1$	$\pi, 1$
$0, 0$	$+$	$-$	$-$	$+$
$\pi, 0$	$-$	$+$	$+$	$-$
$0, 1$	$-$	$+$	$+$	$-$
$\pi, 1$	$+$	$-$	$-$	$+$

FIG. 6. Low-energy spectrum of spin excitations predicted by RPA over a periodic lattice of 1000×1000 iron atoms. Spectral weight is represented by the color code. Hopping parameters are listed in the caption to Fig. 1, while Hund and spin-exchange couplings are set to $J_0 = -100$ meV, $J_1 = 100$ meV, and $J_2 = 50$ meV. The gap maximum is set to $\Delta_0 = 740$ meV, which implies $U_0 = 7.37$ eV by the gap equation, Eq. (22).

and

$$
\begin{bmatrix} \chi_{22}^{+-} & \chi_{23}^{+-} \\ \chi_{32}^{+-} & \chi_{33}^{+-} \end{bmatrix} = \frac{1}{d(2,3)} \begin{bmatrix} \chi_{22}^{(0)+-} & \chi_{23}^{(0)+-} \\ \chi_{32}^{(0)+-} & \chi_{33}^{(0)+-} \end{bmatrix}
$$
$$
\times \begin{bmatrix} 1 - V_3^{+-}\chi_{33}^{(0)+-} & +V_2^{+-}\chi_{23}^{(0)+-} \\ +V_3^{+-}\chi_{32}^{(0)+-} & 1 - V_2^{+-}\chi_{22}^{(0)+-} \end{bmatrix},
$$

(57)

with determinant

$$
d(2,3) = \left(1 - V_2^{+-}\chi_{22}^{(0)+-}\right)\left(1 - V_3^{+-}\chi_{33}^{(0)+-}\right)
$$
$$
- V_2^{+-}V_3^{+-}\chi_{23}^{(0)+-}\chi_{32}^{(0)+-}.
$$

(58)

Above, we have enumerated the indices for true spin, for hidden spin, for the SDW moment, and for the hSDW moment by $1 = (0,0)$, $2 = (\pi, 0)$, $3 = (0, 1)$, and $4 = (\pi, 1)$. These results will be evaluated numerically at low frequency in the next section.

Let us first, however, apply the previous to reveal the Goldstone modes associated with hidden magnetic order (12). Consider then the determinant (56) that describes the dynamics of the principal hidden antiferromagnetic order parameter at small momentum transfer along the x axis: $\boldsymbol{q} = (q_x, 0)$. The factor $1 - V_4^{+-}(\boldsymbol{q})\chi_{44}^{(0)+-}(\boldsymbol{q}, \omega)$ vanishes at $\boldsymbol{q} = 0$ and $\omega = 0$ because of the gap equation (22). After expanding the determinant (56) to lowest nontrivial order in q_x and in ω, we

then get

$$
d(1,4) \cong [1 - U(0)\chi_\perp^{(0)}]\left[-\omega^2 \frac{U(\pi)}{(2\Delta_0)^2}\chi_\perp^{(0)} + q_x^2 \frac{U(\pi)}{(2\Delta_0)^2}\rho_s\right]
$$
$$
- \omega^2 \frac{U(0)U(\pi)}{(2\Delta_0)^2}\chi_\perp^{(0)2}
$$
$$
\cong -\omega^2 \frac{U(\pi)}{(2\Delta_0)^2}\chi_\perp^{(0)} + [1 - U(0)\chi_\perp^{(0)}]q_x^2 \frac{U(\pi)}{(2\Delta_0)^2}\rho_s,
$$

(59)

where

$$
\chi_\perp^{(0)} = \frac{1}{\mathcal{N}}\sum_{\boldsymbol{k}} \frac{\Delta_0^2(\sin 2\delta)^2}{E^3}
$$

(60)

is the bare transverse spin susceptibility [19], and where ρ_s denotes the spin rigidity of the hSDW state. Here, $U(0) = U_0 - \frac{1}{2}J_0 - 4J_1 - 4J_2$ and $U(\pi) = U_0 + \frac{1}{2}J_0$. Setting the determinant to zero, $d(1,4) = 0$, then yields an acoustic dispersion for the Goldstone modes associated with hidden magnetic order, $\omega = c_0|\boldsymbol{q}|$, with a hidden spin wave velocity, $c_0 = (\rho_s/\chi_\perp)^{1/2}$, set by the spin rigidity, ρ_s, and by the transverse spin susceptibility within RPA,

$$
\chi_\perp = \chi_\perp^{(0)}/[1 - U(0)\chi_\perp^{(0)}].
$$

(61)

The former acoustic spectrum for hidden spin waves will be computed numerically in the next section. (See Fig. 6.) Also, substituting in the lowest-order values $\chi_{11}^{(0)+-} \cong \chi_\perp^{(0)}$ and $\chi_{44}^{(0)+-} \cong 1/U(\pi)$ for the matrix elements of the bare spin susceptibility into the RPA expression (55) yields the

dynamical spin susceptibility for hidden spin waves at long wavelength and low frequency:

$$\chi_{44}^{+-}(\boldsymbol{q}, \omega) \cong \frac{(2\langle m_{0,0}\rangle)^2}{\chi_\perp} \frac{1}{c_0^2|\boldsymbol{q}|^2 - \omega^2}, \tag{62}$$

where $\langle m_{0,0}\rangle$ is the ordered moment for the hSDW state (12). We thereby recover the result expected from hydrodynamics for the dynamical correlation function of the antiferromagnetic ordered moment [39,40].

V. NUMERICAL EVALUATION OF RPA

Below, we reveal the spin excitations of the hSDW state within the extended Hubbard model for electron-doped iron selenide over a periodic square lattice of iron atoms. Specifically, the dynamical spin susceptibility is evaluated numerically at half filling within RPA.

A. Propagation along principal axes at low frequency

Let us again suppose that the momentum $\boldsymbol{q}$ carried by a spin excitation in the hSDW state lies along one of the principal axes displayed by Fig. 5. It was demonstrated at the end of the previous section that the RPA solution (50) decouples into dynamics between the true spin and the primary hSDW order parameter (1,4), and into dynamics between the hidden spin and the secondary SDW order parameter (2,3). Equations (55) and (57), specifically, give the respective dynamical spin susceptibilities within RPA. In order to obtain the low-energy spectrum of such spin excitations, we can next expand the bare spin susceptibilities to lowest nontrivial order in frequency. In the case of the dynamics of the primary order parameter, for example, we have

$$\chi_{11}^{(0)+-}(\boldsymbol{q}, \omega) \cong \chi_{11}^{(0)}(\boldsymbol{q}) + \omega^2 \chi_{11}^{(2)}(\boldsymbol{q}), \tag{63}$$

$$\chi_{14}^{(0)+-}(\boldsymbol{q}, \omega) \cong \omega \chi_{14}^{(1)}(\boldsymbol{q}), \tag{64}$$

$$\chi_{44}^{(0)+-}(\boldsymbol{q}, \omega) \cong \chi_{44}^{(0)}(\boldsymbol{q}) + \omega^2 \chi_{44}^{(2)}(\boldsymbol{q}), \tag{65}$$

where $\chi_{11}^{(0)}(\boldsymbol{q}) = \chi_{11}^{(0)+-}(\boldsymbol{q}, 0)$, where $\chi_{44}^{(0)}(\boldsymbol{q}) = \chi_{44}^{(0)+-}(\boldsymbol{q}, 0)$, where

$$\chi_{11}^{(2)}(\boldsymbol{q}) = \frac{1}{\mathcal{N}} \sum_{\boldsymbol{k}} \left(1 - \frac{\varepsilon_+ \varepsilon_+' - \Delta\Delta'}{EE'}\right) \frac{1}{(E+E')^3}$$
$$\times \frac{1}{2}[1 + (\cos 2\delta)(\cos 2\delta') + (\sin 2\delta)(\sin 2\delta')], \tag{66}$$

$$\chi_{44}^{(2)}(\boldsymbol{q}) = \frac{1}{\mathcal{N}} \sum_{\boldsymbol{k}} \left(1 + \frac{\varepsilon_+ \varepsilon_+' + \Delta\Delta'}{EE'}\right) \frac{1}{(E+E')^3}$$
$$\times \frac{1}{2}[1 - (\cos 2\delta)(\cos 2\delta') + (\sin 2\delta)(\sin 2\delta')], \tag{67}$$

and where

$$\chi_{14}^{(1)}(\boldsymbol{q}) = -\frac{1}{\mathcal{N}} \sum_{\boldsymbol{k}} \left(\frac{\Delta}{E} + \frac{\Delta'}{E'}\right) \frac{1}{2} \frac{\sin(2\delta) + \sin(2\delta')}{(E+E')^2}. \tag{68}$$

Recall that we have enumerated the indices for the true spin and for the hidden SDW moment by $1 = (0,0)$ and by $4 = (\pi, 1)$, respectively. The RPA denominator (56) then has the form $d(1,4) = P - \omega^2 Q$, where P and Q are functions of momentum transfer $\boldsymbol{q}$ that are given by

$$P = \left[1 - V_1^{+-} \chi_{11}^{(0)}\right]\left[1 - V_4^{+-} \chi_{44}^{(0)}\right],$$

$$Q = V_1^{+-} \chi_{11}^{(2)}\left[1 - V_4^{+-} \chi_{44}^{(0)}\right] + V_1^{+-} V_4^{+-} \left|\chi_{14}^{(1)}\right|^2$$
$$+ V_4^{+-} \chi_{44}^{(2)}\left[1 - V_1^{+-} \chi_{11}^{(0)}\right]. \tag{69}$$

Setting $d(1,4)$ to zero then yields the approximate energy spectrum of spin excitations, $\omega_b(\boldsymbol{q}) = [P(\boldsymbol{q})/Q(\boldsymbol{q})]^{1/2}$, which is exact in the zero-frequency limit. Also, applying the RPA solution (55) yields the imaginary parts for the dynamical spin susceptibilities of the form $\text{Im}\,\chi_{11}^{+-}(\boldsymbol{q}, \omega) \cong A_{11}(\boldsymbol{q})\delta[\omega - \omega_b(\boldsymbol{q})]$ and $\text{Im}\,\chi_{44}^{+-}(\boldsymbol{q}, \omega) \cong A_{44}(\boldsymbol{q})\delta[\omega - \omega_b(\boldsymbol{q})]$, with respective spectral weights

$$A_{11} = \frac{\pi}{2} \sqrt{\frac{1 - V_4^{+-} \chi_{44}^{(0)}}{1 - V_1^{+-} \chi_{11}^{(0)}}} \frac{\chi_{11}^{(0)}}{Q^{1/2}},$$

$$A_{44} = \frac{\pi}{2} \sqrt{\frac{1 - V_1^{+-} \chi_{11}^{(0)}}{1 - V_4^{+-} \chi_{44}^{(0)}}} \frac{\chi_{44}^{(0)}}{Q^{1/2}}. \tag{70}$$

Similar formulas describe the spin dynamics of the secondary SDW order parameter (2,3). Again, we expand the relevant bare spin susceptibilities to lowest nontrivial order in frequency:

$$\chi_{22}^{(0)+-}(\boldsymbol{q}, \omega) \cong \chi_{22}^{(0)}(\boldsymbol{q}) + \omega^2 \chi_{22}^{(2)}(\boldsymbol{q}), \tag{71}$$

$$\chi_{23}^{(0)+-}(\boldsymbol{q}, \omega) \cong \omega \chi_{23}^{(1)}(\boldsymbol{q}), \tag{72}$$

$$\chi_{33}^{(0)+-}(\boldsymbol{q}, \omega) \cong \chi_{33}^{(0)}(\boldsymbol{q}) + \omega^2 \chi_{33}^{(2)}(\boldsymbol{q}), \tag{73}$$

where $\chi_{22}^{(0)}(\boldsymbol{q}) = \chi_{22}^{(0)+-}(\boldsymbol{q}, 0)$, where $\chi_{33}^{(0)}(\boldsymbol{q}) = \chi_{33}^{(0)+-}(\boldsymbol{q}, 0)$, where

$$\chi_{22}^{(2)}(\boldsymbol{q}) = \frac{1}{\mathcal{N}} \sum_{\boldsymbol{k}} \left(1 - \frac{\varepsilon_+ \varepsilon_+' + \Delta\Delta'}{EE'}\right) \frac{1}{(E+E')^3}$$
$$\times \frac{1}{2}[1 - (\cos 2\delta)(\cos 2\delta') - (\sin 2\delta)(\sin 2\delta')], \tag{74}$$

$$\chi_{33}^{(2)}(\boldsymbol{q}) = \frac{1}{\mathcal{N}} \sum_{\boldsymbol{k}} \left(1 + \frac{\varepsilon_+ \varepsilon_+' - \Delta\Delta'}{EE'}\right) \frac{1}{(E+E')^3}$$
$$\times \frac{1}{2}[1 + (\cos 2\delta)(\cos 2\delta') - (\sin 2\delta)(\sin 2\delta')], \tag{75}$$

and where

$$\chi_{23}^{(1)}(\boldsymbol{q}) = -\frac{1}{\mathcal{N}} \sum_{\boldsymbol{k}} \left(\frac{\Delta}{E} - \frac{\Delta'}{E'}\right) \frac{1}{2} \frac{\sin(2\delta) - \sin(2\delta')}{(E+E')^2}. \tag{76}$$

Again, recall that we have enumerated the indices for the hidden spin and for the true-SDW moment by $2 = (\pi, 0)$ and by $3 = (0, 1)$, respectively. The results for the low-energy spectrum of spin excitations is then identical in form to the previous ones, (69) and (70), but with the replacements of
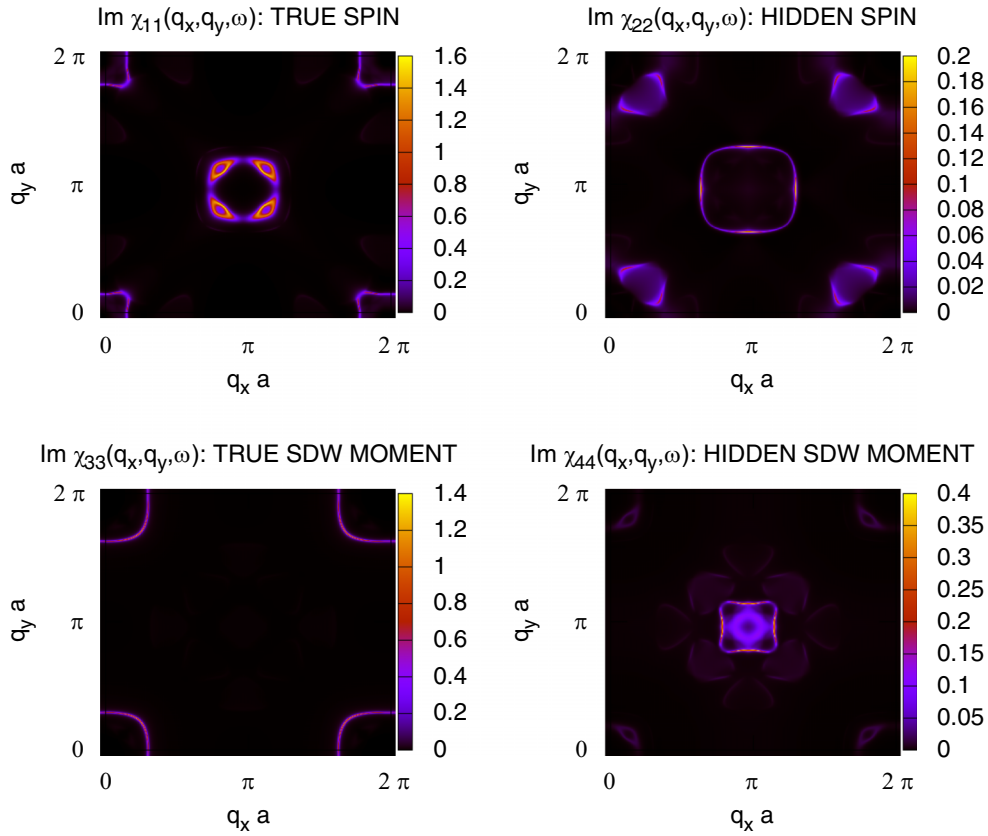
FIG. 7. Spin excitations at frequency $\omega = 350$ meV and damping rate $\Gamma = 16$ meV predicted by RPA over a periodic lattice of 300×300 iron atoms. Hopping parameters are listed in the caption to Fig. 1, while Hund and spin-exchange couplings and the Hubbard U_0 are listed in the caption to Fig. 6.

the true spin with the hidden spin, $1 \rightarrow 2$, and with the replacement of the primary hSDW order parameter with the secondary SDW order parameter, $4 \rightarrow 3$.

Figure 6 displays the spectrum of spin excitations for momenta along a principal axis that is predicted by the low-frequency approximation above. Hopping matrix elements are set to $t_1^{\parallel} = 100$ meV, $t_1^{\perp} = 500$ meV, $t_2^{\parallel} = 0$, and $t_2^{\perp}/i = 100$ meV, while superexchange coupling constants are set to $J_1 = 100$ meV and $J_2 = 50$ meV. Also, the Hund's rule coupling is set to $J_0 = -100$ meV, while the maximum gap is set to $\Delta_0 = 740$ meV. The gap equation (22) thereby implies a Hubbard repulsion $U_0 = 7.37$ eV. Notice that in Fig. 6, the momenta of the dynamical spin susceptibility within the RPA, (55) and (57), have been shifted by the antiferromagnetic nesting vector, $\boldsymbol{Q}_{AF} = (\pi/a, \pi/a)$, for the true SDW-type and for the hidden SDW-type spin excitations. They emerge as poles in frequency of χ_{33}^{+-} and of χ_{44}^{+-}, respectively. The latter hSDW-type excitations notably exhibit the expected Goldstone modes that disperses acoustically from $\boldsymbol{Q}_{AF}$. [See Eq. (62) and Ref. [19].] By contrast, true SDW-type excitations are predicted by RPA near zero momentum at high energy, but they have low spectral weight.

Figure 6 also displays moderately strong excitations near the antiferromagnetic wave vector $\boldsymbol{Q}_{AF}$ in the true-spin channel at high energy. Below, we will see that they form a "floating ring" of spin excitations around $\boldsymbol{Q}_{AF}$. The lowest-energy ones lie along the diagonal axes of the Brillouin zone.

The latter minima of this energy band approach zero energy as the Hund's rule coupling, $|J_0|$, increases. For example, using the set of parameters that correspond to the spin-excitation spectrum displayed by Fig. 6, while maintaining the gap maximum fixed at $\Delta_0 = 740$ meV, the lowest-energy of this band "touches down" to zero energy at a Hund's rule coupling of $J_{0c} = -680$ meV, with a Hubbard repulsion of $U_0 = 7.66$ eV. It is a signal of a quantum phase transition to a different state that obeys Hund's rule, such as the conventional SDW state with nesting vector $\boldsymbol{Q}_{AF}$. The spectrum corresponding to true SDW-type excitations remains unchanged, however, as well as that corresponding to excitations in the hidden-spin channel. Further, increasing the magnetic frustration, J_2, from this point in parameter space moves back up in energy the "floating" ring of magnetic excitations above zero. This confirms the expectation based on the Heisenberg model that magnetic frustration stabilizes the hSDW state versus the true SDW state [21].

B. General wave numbers and frequency

We shall now evaluate the RPA for the dynamical spin susceptibility (50) numerically at a fixed frequency ω and at an artificial damping rate Γ. In particular, the explicit expressions for the bare dynamical spin susceptibility (39)–(48) are evaluated numerically at complex frequency $\omega + i\Gamma$. Figure 7 gives the imaginary part of $\chi^{+-}(\boldsymbol{q}, \omega + i\Gamma)$ at $\omega = 350$ meV and
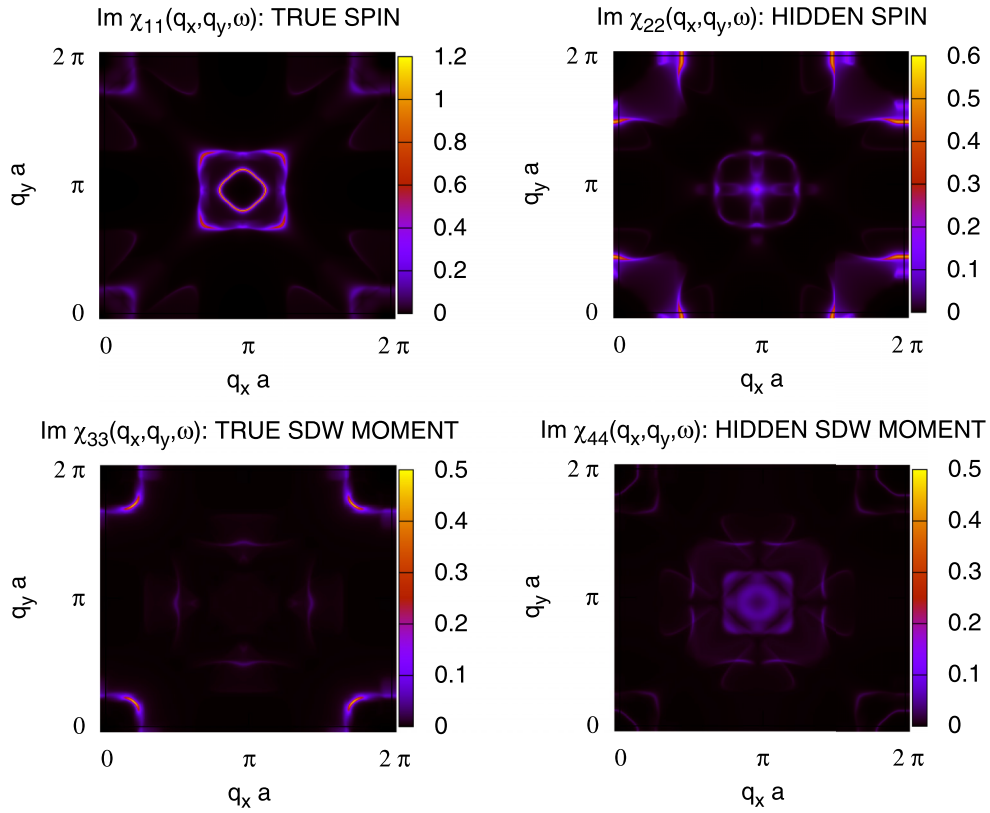
FIG. 8. Spin excitations at frequency $\omega = 500$ meV and damping rate $\Gamma = 16$ meV predicted by RPA over a periodic lattice of 300×300 iron atoms. Hopping parameters, Hund and spin-exchange couplings, and the Hubbard U_0 are identical to those used in Fig. 6.

$\Gamma = 16$ meV. Hopping parameters and interaction parameters are the same as those used in Fig. 1 and in Fig. 6. A smaller periodic square lattice of iron atoms was used, however, with dimensions 300×300. And like in Fig. 6, the momenta of the dynamical spin susceptibility have been shifted by the antiferromagnetic nesting vector, $\boldsymbol{Q}_{\mathrm{AF}} = (\pi/a, \pi/a)$, in the cases of the true-SDW and of the hidden-SDW channels. Notice the moderately strong excitations around the antiferromagnetic wave vector $\boldsymbol{Q}_{\mathrm{AF}}$ in the true-spin channel. They emerge near this frequency, and they therefore coincide with the bottom of the high-energy bands predicted by the low-frequency approximation above, at wave numbers $\boldsymbol{q}$ along a principal axis. (See Fig. 6.) Notice also the vestiges of the Goldstone mode centered at $\boldsymbol{Q}_{\mathrm{AF}}$ in the hSDW channel. Figure 8 shows Im $\chi^{+-}(\boldsymbol{q}, \omega + i\Gamma)$ at the same artificial damping rate, $\Gamma = 16$ meV, but at higher frequency, $\omega = 500$ meV. The Goldstone mode is hardly visible in the hSDW channel, but the high-energy spin excitations in the true-spin channel that circle $\boldsymbol{Q}_{\mathrm{AF}}$ persist. Notice that they now have a "diamond" shape. In summary, the spin-excitation spectrum shows level repulsion at $\omega \sim 300$ meV, which separates Goldstone modes in the hSDW channel at low energy from high-energy modes in the true-spin channel. Both of these types of spin excitations are centered at the antiferromagnetic wave vector, $\boldsymbol{Q}_{\mathrm{AF}}$.

Figure 7 also shows spin excitations around $\boldsymbol{Q}_{\mathrm{AF}}$ in the hidden-spin channel and spin-excitations at the center of the Brillouin zone in the true-SDW channel. As Fig. 6 indicates, these are related by zone folding because of the hSDW background, and they are therefore one and the same. Figure 8 displays that such spin excitations no longer exist at higher energy, however. This is consistent with the collapsed-dome-shaped band at the center of the folded Brillouin zone that is suggested by the low-frequency approximation, Fig. 6, in the hidden-spin and true-SDW channels.

C. Comparison with Heisenberg model

The hSDW state studied above was originally discovered in a local-moment model over a square lattice of iron atoms that contain the principal $d+$ and $d-$ orbitals [17,18,20,21]. The model includes Hund's rule coupling like in H_U (8) and Heisenberg exchange coupling like in H_{sprx} (9). However, separate intraorbital versus interorbital exchange coupling constants, $J_1^{\parallel}$ and $J_1^{\perp}$, exist across nearest neighbors. Spin-wave theory yields that they are related to the spin stiffness of the hSDW state by $J_1^{\parallel} - J_1^{\perp} = \rho_s/2s_0^2$. Spin-wave theory also predicts [19] a "floating ring" of observable spin excitations around $\boldsymbol{Q}_{\mathrm{AF}}$. However, as Hund's rule coupling $-J_0$ increases, the hSDW is eventually destabilized by a "stripe" SDW that intervenes. By comparison, the above RPA calculation does not indicate that the hSDW state is destabilized by the "stripe" SDW state as Hund's rule is enforced. This discrepancy could be due to the fact that the local-moment model assumes infinitely strong Hubbard repulsion, U_0, while keeping the Hund's rule coupling, $-J_0$, finite. Nonetheless, both the present RPA treatment and the previous local-moment model find that the hSDW state eventually becomes unstable as Hund's rule is enforced, as expected.

VI. DISCUSSION AND CONCLUSIONS

Inelastic neutron scattering studies of alkali-atom-intercalated FeSe and of organic-molecule-intercalated FeSe find evidence for low-energy spin excitations not at, but around, the wave vector $(\pi/a, \pi/a)$ in the unfolded (one-iron) Brillouin zone [8–12]. In particular, the lowest-energy spin excitations that have been observed in the superconducting state lie just below the gap in energy for quasiparticle excitations, $2\Delta_{\mathrm{SC}} \cong 28$ meV, at wave vectors that lie midway between that corresponding to "stripe" SDW order and that corresponding to Néel order. Interestingly, evidence exists for low-energy spin excitations in the normal state of such electron-doped iron selenides [11], at wave numbers near $(\pi/a, \pi/a)$. In particular, spin excitations that form a "diamond" around this wave vector exist at energy scales above the gap in organic-molecule-intercalated iron selenide high-temperature superconductors [11].

The hSDW state studied here ideally exists at half filling. It may therefore provide a good description of the normal state in electron-doped FeSe high-T_c superconductors. Figures 7 and 8 summarize the predictions for the nature of high-energy spin excitations within RPA. The true-spin channel is most likely the only one that is observable by neutron scattering. It shows a "floating ring" of spin excitations around the antiferromagnetic wave vector $\mathbf{Q}_{\mathrm{AF}}$ that begins at a threshold energy (Fig. 7), followed by spin excitations at higher energy that form a "diamond" around the same wave vector (Fig. 8). Inelastic neutron scattering on electron-doped iron selenide indicates that relatively high-energy magnetic resonances exist above the quasiparticle energy gap, in the range 80–130 meV, at wave numbers that roughly form a diamond around the same wave vector [11]. Note that the threshold energy of the "floating ring" shown by Fig. 7 is three times larger. It can be reduced, however, by increasing the Hund's rule coupling toward $|J_{0c}|$, at which the threshold collapses to zero energy. The qualitative agreement of theory with experiment suggests that hidden magnetic order of the type studied here exists in electron-doped iron selenide.

In summary, we have studied the nature of low-energy spin excitations due to hidden magnetic order in an extended Hubbard model for a single layer of iron selenide. The Hubbard model notably contains only the two principal $3d_{xz}$ and $3d_{yz}$ orbitals of the iron atom. An RPA was developed along the lines of the "spin bag" calculation for the SDW state of the conventional Hubbard model over the square lattice by Schrieffer, Wen, and Zhang [26–29]. It predicts an observable "diamond" of spin excitations around the nesting vector of the hSDW state, $\mathbf{Q}_{\mathrm{AF}} = (\pi/a, \pi/a)$, at energies above the band of Goldstone modes, which are not observable. Such "hollowed-out" spin excitations at $\mathbf{Q}_{\mathrm{AF}}$ have been observed by inelastic neutron scattering in bulk electron-doped iron selenide [9,11]. The present RPA calculations also predict that they move down in energy as Hund's rule is enforced, while that they move up in energy with increasing magnetic frustration.

Absent from the mean-field/RPA study of the hSDW state presented above is a description of the superconducting state in electron-doped iron selenide. Maier and co-workers have proposed that a nodeless D-wave paired state accounts for the spin resonances that lie at energies inside the quasiparticle gap in electron-doped iron selenide [9,11,41]. Mazin argued, however, that a true node appears after zone-folding the one-iron Brillouin zone because of hybridization between the two inequivalent iron sites in [42] FeSe. ARPES finds no evidence for gap nodes [14,15], on the other hand. The author has recently found an instability to S-wave pairing in the hSDW state upon electron doping, where the sign of the Cooper pair wave function alternates between electron pockets and faint hole pockets [22]. Such electron/hole pockets lie at the corner of the folded Brillouin zone, and they are due to a Lifshitz transition of the Fermi surfaces that is incited by fluctuation exchange with the Goldstone modes associated with hidden magnetic order (62). (See Fig. 3 and Ref. [19].) It remains to be seen what type of low-energy spin resonance is predicted by such an S^{+-} paired state.

APPENDIX A: ORBITAL MATRIX ELEMENTS

The operators that create the eigenstates (4) of the electron hopping Hamiltonian, H_{hop}, are

$$c_s^\dagger(n, \mathbf{k}) = \mathcal{N}^{-1/2} \sum_i \sum_{\alpha=0,1} (-1)^{\alpha n} e^{i(2\alpha-1)\delta(\mathbf{k})} e^{i\mathbf{k}\cdot\mathbf{r}_i} c_{i,\alpha,s}^\dagger, \tag{A1}$$

where $\alpha = 0$ and 1 index the $d-$ and $d+$ orbitals, and where $n = 1$ and 2 index the antibonding and bonding orbitals $(-i)d_{y(\delta)z}$ and $d_{x(\delta)z}$. The inverse of the above is then

$$c_{i,\alpha,s}^\dagger = \mathcal{N}^{-1/2} \sum_{\mathbf{k}} \sum_{n=1,2} (-1)^{\alpha n} e^{-i(2\alpha-1)\delta(\mathbf{k})} e^{-i\mathbf{k}\cdot\mathbf{r}_i} c_s^\dagger(n, \mathbf{k}). \tag{A2}$$

Plugging (A2) and its Hermitian conjugate into the expression for the electron spin density wave operator,

$$\mathbf{S}(m\pi, \mathbf{q}) = \frac{1}{2} \sum_s \sum_{s'} \sum_i \sum_\alpha (-1)^{m\alpha} e^{i\mathbf{q}\cdot\mathbf{r}_i} c_{i,\alpha,s}^\dagger \boldsymbol{\sigma}_{s,s'} c_{i,\alpha,s'}, \tag{A3}$$

yields the form

$$S(m\pi, \boldsymbol{q}) = \frac{1}{2} \sum_s \sum_{s'} \sum_{\boldsymbol{k}} \sum_{n,n'} \mathcal{M}_{n,\boldsymbol{k};n',\boldsymbol{k}'} c_s^\dagger(n',\boldsymbol{k}')\sigma_{s,s'}c_{s'}(n,\boldsymbol{k}), \tag{A4}$$

with matrix element

$$\mathcal{M}_{n,\boldsymbol{k};n',\boldsymbol{k}'} = \frac{1}{2} \sum_{\alpha=0,1} e^{i(2\alpha-1)[\delta(\boldsymbol{k})-\delta(\boldsymbol{k}')]}(-1)^{(n'-n+m)\alpha}. \tag{A5}$$

Here, $m = 0$ or 1, and $\boldsymbol{k}' = \boldsymbol{k} + \boldsymbol{q}$. The matrix element therefore equals [19]

$$\mathcal{M}_{n,\boldsymbol{k};n',\boldsymbol{k}'} = \begin{cases} \cos[\delta(\boldsymbol{k}) - \delta(\boldsymbol{k}')], & \text{for} \quad n' = n + m \ (\text{mod } 2), \\ -i\sin[\delta(\boldsymbol{k}) - \delta(\boldsymbol{k}')], & \text{for} \quad n' = n + m + 1 \ (\text{mod } 2). \end{cases} \tag{A6}$$

APPENDIX B: TRACE FORMULAS FOR PRODUCTS OF 2 × 2 MATRICES

Below, we compute the trace of the product of 2×2 matrices $\text{tr}(\tau_\mu \tau_\gamma \tau_\nu \tau_\delta)$, where τ_0 is the identity matrix, and where τ_1, τ_2, and τ_3 are Pauli matrices. The indices μ and ν pertain to the Nambu-Gorkov Green's function: $G = \sum_{\mu=0}^3 G^{(\mu)}\tau_\mu$. We will exploit the product rule obeyed by Pauli matrices:

$$\tau_i \tau_j = \delta_{i,j}\tau_0 + i\sum_{k=1}^3 \epsilon_{i,j,k}\tau_k. \tag{B1}$$

Throughout, Greek-letter indices run through 0, 1, 2, and 3, while Latin-letter indices run through 1, 2, and 3.

(1) $\text{tr}(\tau_\mu \tau_0 \tau_\nu \tau_0) = \text{tr}(\tau_\mu \tau_\nu) = 2\delta_{\mu,\nu}$.

(2) $\text{tr}(\tau_\mu \tau_i \tau_\nu \tau_i) = 2\,\text{sgn}_\mu(i)\delta_{\mu,\nu}$,

where $\text{sgn}_\mu(i) = 1$ if $\mu = 0$ or i, and where $\text{sgn}_\mu(i) = -1$ otherwise.

(3) $\text{tr}(\tau_\mu \tau_0 \tau_\nu \tau_i) = \text{tr}(\tau_\mu \tau_\nu \tau_i) = 2(\delta_{\mu,0}\delta_{\nu,i} + \delta_{\mu,i}\delta_{\nu,0} + i\epsilon_{\mu,\nu,i})$,

where $\epsilon_{\mu,\nu,i}$ coincides with the Levi-Civita tensor for $\mu, \nu = 1, 2, 3$, while it vanishes otherwise, for $\mu = 0$, or for $\nu = 0$.

(4) $\text{tr}(\tau_\mu \tau_i \tau_\nu \tau_0) = \text{tr}(\tau_\mu \tau_i \tau_\nu) = 2(\delta_{\mu,0}\delta_{\nu,i} + \delta_{\mu,i}\delta_{\nu,0} + i\epsilon_{\mu,i,\nu})$,

where $\epsilon_{\mu,i,\nu}$ coincides with the Levi-Civita tensor for $\mu, \nu = 1, 2, 3$, while it vanishes otherwise, for $\mu = 0$, or for $\nu = 0$.

(5) $\text{tr}(\tau_\mu \tau_i \tau_\nu \tau_j) = 2(\delta_{\mu,i}\delta_{\nu,j} + \delta_{\mu,j}\delta_{\nu,i} + i\delta_{\mu,0}\epsilon_{i,\nu,j} + i\delta_{\nu,0}\epsilon_{\mu,i,j})$ for $i \neq j$,

where $\epsilon_{i,\nu,j}$ and $\epsilon_{\mu,i,j}$ coincide with the Levi-Civita tensor for $\mu, \nu = 1, 2, 3$, while they vanish otherwise, for $\mu = 0$, or for $\nu = 0$.

Importantly, notice that the matrix formed by the trace as a function of the indices γ and δ is Hermitian:

$$\text{tr}(\tau_\mu \tau_\gamma \tau_\nu \tau_\delta) = \text{tr}(\tau_\mu \tau_\delta \tau_\nu \tau_\gamma)^*.$$

[1] H. F. Fong, B. Keimer, P. W. Anderson, D. Reznik, F. Dogan, and I. A. Aksay, Phonon and Magnetic Neutron Scattering at 41 meV in YBa$_2$Cu$_3$O$_7$, Phys. Rev. Lett. **75**, 316 (1995).

[2] D. S. Inosov, J. T. Park, P. Bourges, D. L. Sun, Y. Sidis, A. Schneidewind, K. Hradil, D. Haug, C. T. Lin, B. Keimer, and V. Hinkov, Normal-state spin dynamics and temperature-dependent spin-resonance energy in optimally doped BaFe$_{1.85}$Co$_{0.15}$As$_2$, Nat. Phy. **6**, 178 (2010).

[3] M. M. Korshunov and I. Eremin, Theory of magnetic excitations in iron-based layered superconductors, Phys. Rev. B **78**, 140509(R) (2008).

[4] T. A. Maier and D. J. Scalapino, Theory of neutron scattering as a probe of the superconducting gap in the iron pnictides, Phys. Rev. B **78**, 020514(R) (2008).

[5] I. I. Mazin, D. J. Singh, M. D. Johannes, and M. H. Du, Unconventional Superconductivity with a Sign Reversal in the Order Parameter of LaFeAsO$_{1-x}$F$_x$, Phys. Rev. Lett. **101**, 057003 (2008).

[6] K. Kuroki, S. Onari, R. Arita, H. Usui, Y. Tanaka, H. Kontani, and H. Aoki, Unconventional Pairing Originating from the Disconnected Fermi Surfaces of Superconducting LaFeAsO$_{1-x}$F$_x$, Phys. Rev. Lett. **101**, 087004 (2008).

[7] S. Graser, T. A. Maier, P. J. Hirschfeld, and D. J. Scalapino, Near-degeneracy of several pairing channels in multiorbital models for the Fe pnictides, New J. Phys. **11**, 025016 (2009).

[8] J. T. Park, G. Friemel, Yuan Li, J.-H. Kim, V. Tsurkan, J. Deisenhofer, H.-A. Krug von Nidda, A. Loidl, A. Ivanov, B. Keimer, and D. S. Inosov, Magnetic Resonant Mode in the Low-Energy Spin-Excitation Spectrum of Superconducting Rb$_2$Fe$_4$Se$_5$ Single Crystals, Phys. Rev. Lett. **107**, 177005 (2011).

[9] G. Friemel, J. T. Park, T. A. Maier, V. Tsurkan, Yuan Li, J. Deisenhofer, H.-A. Krug von Nidda, A. Loidl, A. Ivanov, B. Keimer, and D. S. Inosov, Reciprocal-space structure and dispersion of the magnetic resonant mode in the superconducting phase of Rb$_x$Fe$_{2-y}$Se$_2$ single crystals, Phys. Rev. B **85**, 140511(R) (2012).

[10] N. R. Davies, M. C. Rahn, H. C. Walker, R. A. Ewings, D. N. Woodruff, S. J. Clarke, and A. T. Boothroyd, Spin resonance in the superconducting state of $Li_{1-x}Fe_xODFe_{1-y}Se$ observed by neutron spectroscopy, Phys. Rev. B **94**, 144503 (2016).

[11] B. Pan, Y. Shen, D. Hu, Y. Feng, J. T. Park, A. D. Christianson, Q. Wang, Y. Hao, H. Wo, Z. Yin, T. A. Maier, and J. Zhao, Structure of spin excitations in heavily electron-doped $Li_{0.8}Fe_{0.2}ODFeSe$ superconductors, Nat. Commun. **8**, 123 (2017).

[12] M. Ma, L. Wang, P. Bourges, Y. Sidis, S. Danilkin, and Y. Li, Low-energy spin excitations in $(Li_{0.8}Fe_{0.2})ODFeSe$ superconductor studied with inelastic neutron scattering, Phys. Rev. B **95**, 100504(R) (2017).

[13] S. He, J. He, W.-H. Zhang, L. Zhao, D. Liu, X. Liu, D. Mou, Y.-B. Ou, Q.-Y. Wang, Z. Li, L. Wang, Y. Peng, Y. Liu, C. Chen, L. Yu, G. Liu, X. Dong, J. Xhang, C. Chen, Z. Xu, X. Chen, X. Ma, Q. Xue, and X. J. Zhou, Phase diagram and electronic indication of high-temperature superconductivity at 65 K in single-layer FeSe films, Nat. Mater. **12**, 605 (2013).

[14] R. Peng, X. P. Shen, X. Xie, H. C. Xu, S. Y. Tan, M. Xia, T. Zhang, H. Y. Cao, X. G. Gong, J. P. Hu, B. P. Xie, and D. L. Feng, Measurement of an Enhanced Superconducting Phase and a Pronounced Anisotropy of the Energy Gap of a Strained FeSe Single Layer in FeSe/Nb: $SrTiO_3/KTaO_3$ Heterostructures Using Photoemission Spectroscopy, Phys. Rev. Lett. **112**, 107001 (2014).

[15] J. J. Lee, F. T. Schmitt, R. G. Moore, S. Johnston, Y.-T. Cui, W. Li, M. Yi, Z. K. Liu, M. Hashimoto, Y. Zhang, D. H. Lu, T. P. Devereaux, D.-H. Lee, and Z.-X. Shen, Interfacial mode coupling as the origin of the enhancement of T_c in FeSe films on $SrTiO_3$, Nature (London) **515**, 245 (2014).

[16] L. Zhao, A. Liang, D. Yuan, Y. Hu, D. Liu, J. Huang, S. He, B. Shen, Y. Xu, X. Liu, L. Yu, G. Liu, H. Zhou, Y. Huang, X. Dong, F. Zhou, Z. Zhao, C. Chen, Z. Xu, and, X. J. Zhou, Common electronic origin of superconductivity in (Li, Fe)OHFeSe bulk superconductor and single-layer $FeSe/SrTiO_3$ films, Nat. Commun. **7**, 10608 (2016).

[17] J. P. Rodriguez, Isotropic Cooper pairs with emergent sign changes in a single-layer iron superconductor, Phys. Rev. B **95**, 134511 (2017).

[18] J. P. Rodriguez, Particle-hole transformation in strongly-doped iron-based superconductors, Symmetry **11**, 396 (2019).

[19] J. P. Rodriguez and R. Melendrez, Fermi surface pockets in electron-doped iron superconductor by Lifshitz transition, J. Phys. Commun. **2**, 105011 (2018); Corrigendum: Fermi surface pockets in electron-doped iron superconductor by Lifshitz transition, **3**, 019501 (2019).

[20] J. P. Rodriguez and E. H. Rezayi, Low Ordered Magnetic Moment by Off-Diagonal Frustration in Undoped Parent Compounds to Iron-Based High-T_c Superconductors, Phys. Rev. Lett. **103**, 097204 (2009).

[21] J. P. Rodriguez, Magnetic excitations in ferropnictide materials controlled by a quantum critical point into hidden order, Phys. Rev. B **82**, 014505 (2010).

[22] J. P. Rodriguez, Superconductivity by hidden spin fluctuations in electron-doped iron selenide, arXiv:2001.07908.

[23] Y. Nambu, Quasiparticles and gauge invariance in the theory of superconductivity, Phys. Rev. **117**, 648 (1960).

[24] L. P. Gorkov, Ob energeticheskom spektre sverkhprovodnikov, Zh. Eksp. Teor. Fiz. **34**, 735 (1958); [About the energy spectrum of superconductors, Sov. Phys. JETP **7**, 505 (1958)].

[25] J. R. Schrieffer, *Theory of Superconductivity* (Benjamin, New York, 1964).

[26] J. E. Hirsch, Two-dimensional Hubbard model: Numerical simulation study, Phys. Rev. B **31**, 4403 (1985).

[27] J. R. Schrieffer, X. G. Wen, and S. C. Zhang, Dynamic spin fluctuations and the bag mechanism of high-T_c superconductivity, Phys. Rev. B **39**, 11663 (1989).

[28] A. Singh and Z. Tesanovic, Collective excitations in a doped antiferromagnet, Phys. Rev. B **41**, 614 (1990).

[29] A. V. Chubukov and D. M. Frenkel, Renormalized perturbation theory of magnetic instabilities in the two-dimensional Hubbard model at small doping, Phys. Rev. B **46**, 11884 (1992).

[30] S. Raghu, X.-L. Qi, C.-X. Liu, D. J. Scalapino, and Shou-Cheng Zhang, Minimal two-band model of the superconducting iron oxypnictides, Phys. Rev. B **77**, 220503(R) (2008).

[31] P. A. Lee and X.-G. Wen, Spin-triplet p-wave pairing in a three-orbital model for iron pnictide superconductors, Phys. Rev. B **78**, 144517 (2008).

[32] J. P. Rodriguez, M. A. N. Araujo, and P. D. Sacramento, Emergent nesting of the Fermi surface from local-moment description of iron-pnictide high-T_c superconductors, Eur. Phys. J. B **87**, 163 (2014).

[33] P. W. Anderson, Antiferromagnetism: Theory of superexchange interaction, Phys. Rev. **79**, 350 (1950).

[34] Q. Si and E. Abrahams, Strong Correlations and Magnetic Frustration in the High-T_c Iron Pnictides, Phys. Rev. Lett. **101**, 076401 (2008).

[35] M. Daghofer, A. Moreo, J. A. Riera, E. Arrigoni, D. J. Scalapino, and E. Dagotto, Model for the Magnetic Order and Pairing Channels in Fe Pnictide Superconductors, Phys. Rev. Lett. **101**, 237004 (2008); A. Moreo, M. Daghofer, J. A. Riera, and E. Dagotto, Properties of a two-orbital model for oxypnictide superconductors: Magnetic order, B_{2g} spin-singlet pairing channel, and its nodal structure, Phys. Rev. B **79**, 134502 (2009).

[36] C. Xu, M. Müller, and S. Sachdev, Ising and spin orders in the iron-based superconductors, Phys. Rev. B **78**, 020501(R) (2008).

[37] M. Yoshizawa and S. Simayi, Anomalous elastic behavior and its correlation with superconductivity in iron-based superconductor $Ba(Fe_{1-x}Co_x)_2As_2$, Mod. Phys. Lett. B **26**, 1230011 (2012).

[38] E. Berg, M. A. Metlitski, and S. Sachdev, Sign-problem-free quantum Monte Carlo of the onset of antiferromagnetism in metals, Science **338**, 1606 (2012).

[39] B. I. Halperin and P. C. Hohenberg, Hydrodynamic theory of spin waves, Phys. Rev. **188**, 898 (1969).

[40] D. Forster, *Hydrodynamic Fluctuations, Broken Symmetry, and Correlation Functions* (Benjamin/Cummings, Reading, MA, 1975).

[41] T. A. Maier, S. Graser, P. J. Hirschfeld, and D. J. Scalapino, d-wave pairing from spin fluctuations in the $K_xFe_{2-y}Se_2$ superconductors, Phys. Rev. B **83**, 100515(R) (2011).

[42] I. I. Mazin, Symmetry analysis of possible superconducting states in $K_xFe_ySe_2$ superconductors, Phys. Rev. B **84**, 024529 (2011).